Passive Wireless Resonator Sensor for the Measurement of AC Electric Field

by

Mana Yazdani

A thesis submitted to the Faculty of Graduate Studies of
the University of Manitoba
in partial fulfillment of the requirements for the degree of

Doctor of Philosophy

Department of Electrical and Computer Engineering
University of Manitoba
Winnipeg, Canada

Abstract

A passive wireless sensor is designed, fabricated and tested for the measurement of AC electric field in the vicinity of high voltage apparatus. This sensor is applicable in remote condition monitoring of high voltage apparatus where close distance measurements raises safety hazards for operators. The sensor is designed using a coaxial cavity resonator structure (in TEM mode) capacitively coupled to varactors. The resonance frequency of the sensor shifts corresponding to the capacitance variation of the varactors which in turn is perturbed by the external electric field. The electric field surrounding the apparatus induces a bias voltage over the terminals of the varactors. Therefore, the resonance frequency changes proportional to the inducing external electric field and correspondingly to the medium/high voltage. A printed circuit board on the top of the cavity provides coupling between the cavity and varactors and also between the varactors and the external field produced by the high voltage apparatus. The sensor structure is designed to resonate in the range of 2.4 GHz to 2.5 GHz of the industrial, scientific and medical (ISM) radio frequency band. A remote interrogation system identifies the instantaneous resonance frequency of the sensor by transmitting pulses of radio frequency (RF) signal and recording the ring back of the resonator. The ring back is down converted and analyzed to determine the resonance frequency of the sensor. Two possible applications of the sensor, *i.e.* voltage measurement and defect detection of insulators, are demonstrated by experimental results.

Acknowledgements

I would like to express my sincere gratitude to my advisor Dr. Behzad Kordi for his continuous support through my Ph.D. studies. His encouraging advice with tremendous patience has motivated me throughout my work. I would also like to thank my co-advisor, Dr. Douglas J. Thomson, for his insightful comments and suggestions through my research. I could not have imagined better advisors and mentors for my Ph.D. research.

Besides my advisors, I would like to thank my thesis committee, Dr. Greg E. Bridges and Dr. Dagmar Svecova for their valuable comments and questions which motivated a wider and deeper study of the research work.

I am grateful to Dr. Farhad Rachidi for accepting to be the external examiner of my PhD thesis and evaluating my work. His insightful comments improved the quality of the thesis.

Many thanks to Dr. David Swatek from Manitoba Hydro for being the advocate of this project and sharing his broad knowledge of the industry. He has had a great influence on this work by his ideas on specific applications of the work. Financial support from Manitoba Hydro and Mitacs is gratefully appreciated.

I would also like to acknowledge the time and effort that the technicians at the University of Manitoba have put into this work. Thanks to Daryl Hamelin and Cory Smit, many of my brain storming ideas have turned into actual reality. Thanks to Mr. Daniel Card who has spent hours explaining the available technologies to me, I saved a significant amount of time learning from his experience.

Last but not least, I would like to thank my family and friends. My husband, Mohammad Goulkhah, has always been there for me discussing the overwhelming technical barriers. Many of the ideas in my thesis work has originated from our long discussions. My parents, Guity Khadjehzadeh and Manuchehr Yazdani, and my sister, Maryam Yazdani, have always supported and encouraged me throughout my Ph.D. work and life in general.

Table of Contents

List of Figures

List of Tables

Chapter 1

Introduction

The increasing demand for electric power over the last decade has resulted in high voltage apparatus to operate at full load while the power systems are expected to provide high quality and reliable electric power. In addition, the increasing dependence on the electricity has increased the cost of power outages and quality disturbances [1]. In order to avoid power outages and disturbances caused by equipment failures and outages, online distributed and low-cost condition monitoring, diagnostics, and protections are crucial in modern power systems [2, 3].

Electric field measurement in the vicinity of high voltage apparatus is part of condition monitoring and protection in power systems. Determining the electric field distribution profile surrounding high voltage equipment provides reliability information about the insulation condition [4, 5]. This information will enhance the safety of the human resources and the equipment in live line maintenance [6]. As another application, the voltage of the high voltage device can be derived based on the measured electric field profile [7].

In this chapter, the difficulties of using the available electric field measurement methods are mentioned. Then, the electric field sensor is introduced to overcome the issues pertinent to the conventional methods.

1.1 Problem Statement

Unlike low voltage electrical systems, condition monitoring of high voltage devices involves complicated difficulties. The voltage difference between the high voltage devices and the ground will induce high electric field around them. Safety of the personnel dealing with the monitoring devices in the vicinity of these high electric fields must be provided. As a result, remote access to the monitoring systems is desired. The conventional measurement devices for monitoring the operational parameters of high voltage apparatus such as voltage and current are based on transformers and voltage dividers. These devices are attached to the high voltage apparatus and reduce the voltage or current to a level that is measurable by the low voltage and current measurement equipment. On the other hand, high voltages are usually measured by bulky voltage dividers which consist of a combination of resistors, capacitors and transformers. The employment of these components introduces certain limitations to the measurement results. Saturation of transformers is an example of such limitations [8]. The general deficiencies imposed by these measurement methods are power dissipation and source loading caused by direct attachment to the high voltage apparatus. Additionally, the resistors, capacitors and transformers are subjected to temperature effects which develop inaccuracies. Another issue initiated by the application of transformers in the measurement circuits is the induction of ferro-resonance in power systems [9]. Also, these components require high insulation for safety measures. The insulation is usually provided by paper-oil or SF_6 gas. Deterioration of the paper-oil insulation introduced by aging imposes technical difficulties such as regular changing and extra costs. Further, SF_6 is the focus of many researchers to be substituted by other environmental friendly materials [10].

1.2 Objectives

The objective of this PhD thesis was to design and fabricate a passive, wireless electric field sensor and a compatible interrogation system. The sensor is employed in the measurement of electric field in the vicinity of high voltage apparatus. The sensor is composed of a coaxial resonator loaded with varactors which are lumped elements with variable capacitance changing based on the applied reverse bias voltage across the element terminals. The sensor is interrogated remotely by sending radio frequency (RF) pulses.

The sensor is passive meaning no battery is required. It is small, light weight and inexpensive which makes it easy to utilize in distributed measurements around high voltage apparatus. The sensor does not require grounding, therefore it can be mounted in close distance from the high voltage apparatus. The measurement information of the sensor could optionally be employed in condition monitoring of high voltage apparatus, such as locating insulation defects. Further, a distributed array of sensors can be employed in measuring the electric field profile surrounding the high voltage apparatus and deriving the inducing medium/high voltage of the apparatus.

1.3 Research Outcomes and Contributions

A passive, light weight and inexpensive electric field sensor and a compatible interrogation system was designed, fabricated, and tested. The sensor consists of a coaxial transmission line cavity resonator built out of copper tubes. It is designed and simulated by finite element simulation tools and the performance of the fabricated sensor is evaluated through a variety of experiment to measure electric field profiles in the vicinity of high voltage apparatus.

The sensor is operable in close proximity of high voltage apparatus and is used in remote measurement of electric field and medium/high voltage. Unlike most sensors, the passive sensor will not require energy harvesting from the high voltage apparatus, hence, eliminat-

ing the technical complications pertinent to direct connection of the existing measurement devices to the high voltage apparatus.

The interrogation system, which is compatible with the resonator sensor, is composed of RF generators and switches. The data from the sensor is received wirelessly and captured on a fast digital oscilloscope which can be replaced by a data acquisition circuit in the future. The wireless interrogation of the sensor provides a safe distance from the high voltage apparatus for the operators.

The measurement method introduced in this thesis combines the advantages of the existing electric field and high voltage measurement methods. Moreover, the application of the sensor for medium/high voltage measurement in addition to the detection of insulation defects are demonstrated by deriving the electric field profile surrounding the high voltage devices. The measurement method is capable of measuring the AC electric field or voltage variation while some of the new techniques are only capable of measuring the root mean square (RMS) value [11, 12]. The conventional high voltage measurement methods are composed of transformers and voltage dividers which require direct electrical attachment to the apparatus [8]. Recently, electric field and voltage measurement methods using sensors have been proposed to overcome the loading issues imposed by the conventional methods. The new methods are either dependent on energy harvesting from the apparatus [11,12] or require wired (*e.g.* electrical, optical) connection to an interrogation system [13,14]. The existing measurement techniques are further discussed in the next chapter.

1.3.1 Publications

A PCT international patent has been filed on the proposed sensor in this thesis [15] and the outcomes of this research have been published in two conference papers [16, 17] and one journal paper [18]. The details of the interrogation system has been published in [16]. A voltage measurement method using the electric field sensors is proposed in [17] and

the corresponding measurement results are reported in the paper. The journal paper in [18] is about the design and implementation of the electric field sensor. Another journal paper discussing the application of the sensor in the detection of insulation defects will be submitted.

Chapter 2

Electric Field Sensors and Wireless Interrogation Systems–A Literature Review

Electric field sensors and probes are employed in different applications depending on their measurable range. The electric field sensors applicable in the vicinity of high voltage apparatus have a wide variety and require electrical isolation from the high voltage apparatus or the ground to avoid flashover caused by close proximity of high voltage and ground. In order to provide the electrical isolation, some of these electric field sensors are placed close to the high voltage apparatus as floating objects and interrogated remotely.

Passive wireless sensors are emerging to resolve measurement problems where contactless measurement is advantageous. A group of these sensors are resonators with variable resonance frequency. Remote interrogation method of these sensors varies depending on the type of sensor. Most of these sensors are measuring slow varying measurands. The available electric field measurement systems along with the remote interrogation methods of resonator-based sensors are discussed in this chapter.

2.1 Electric Field Sensors and Probes for High Voltage Applications

The electric field sensors and probes employed in the measurement of electric field in the vicinity of high voltage apparatus are used for condition monitoring, power system protection, voltage measurement and detection of insulation defects. Determining the electric field distribution profile surrounding high voltage equipment provides reliability information about the insulation condition [4, 5, 19–21]. This information will enhance the safety of human resources and the equipment in live line maintenance [6]. As a further application, the voltage of the high voltage device can be derived based on the measured electric field profile [7, 11, 12]. The electric field sensors and probes used in high voltage applications and their pros and cons are briefly discussed in the following sections.

2.1.1 Optical Electric Field Sensors and Probes

One of the most popular electric field sensors and probes employed in the measurements of high voltages are the optical sensors. The fiber structure of these sensors provides electrical isolation from high voltage that is required for safety measures. These sensors operate based on the Pockels or Kerr effects defined as the variation in an optical medium in response to a variation in an external electric field [22, 23].

The optical sensors and probes are employed in voltage measurement as a substitute for potential transformers [14, 24]. Unlike conventional potential transformers, the optical voltage transducers are electrically isolated from the high voltage device and have no loading effect. An insulator is required to hold the optical sensors and probes in close distance from high voltage apparatus which increases the size and the weight of the optical voltage transducer to a few hundreds of kilograms [14].

Another application of optical probes is in insulation defect detection [25–27]. Although

these sensors provide electrical isolation from the high voltage apparatus required for the safety measures, they are directly connected to an interrogation system by optical fibers. This direct connection complicates the usage of these sensors in the live-line maintenance.

The optical sensors typically have high resolution (*i.e.* 0.7 V/m/$\sqrt{\text{Hz}}$), high operating bandwidth (*i.e.* 1 kHz-10 GHz) and a wide range of measurable electric field (*i.e.* up to 100 kV/m) [26, 27]. However, these sensors are active (*i.e.* need a source of power) and require direct connection to an interrogation system.

2.1.2 Micromachined Electric Field Mills

Micro-machined electric field mill sensors commonly known as MEMS (Micro–Electro–Mechanical Sensors) are another group of electric field sensors employed in the measurement of AC or DC electric fields. These sensors have a complicated fabrication procedure and are recently being studied to be used in high voltage measurements [28–30]. The sensors reported in [28, 29, 31–34] operate by thermal actuators. The induced electric field on the sensor causes heating which in turn results in the displacement of the sensor shutters. This displacement is either sensed by laser beam deflection or by capacitive monitoring. In the former case, a displacement in the sensor shutter causes a deviation in the reflected laser beam on the shutter and for the latter, the capacitive change due to the displacement of the electrodes is measured by an electrical circuit. The reported measurable range for these sensors is 100 V/m − 500kV/m and the prototypes have been tested for DC electric field measurements. These sensors are active and require direct electrical connection to an interrogation system which limits the application of these sensors for measurements in the vicinity of high voltage apparatus.

2.1.3 Electrostatic Probes

Different types of electrostatic probes are used in the vicinity of high voltage apparatus. Some of the contactless electrostatic probes are employed in sensing the presence of the voltage in order to verify complete electrical isolation of the equipment under maintenance. There are other contactless probes that are used for determining the range of voltage (*e.g.* in the ranges of 120 V_{rms}-1.2 kV_{rms}, 1.2 $\text{kV}_{\text{rms}} - 2.2\,\text{kV}_{\text{rms}}$, and up to 500 kV_{rms}) on a medium or high voltage device [35]. These contactless probes are typically mobile measurement devices operated by batteries. Hence, the resolution of the measured voltage is in the range of kilo-$\text{volts}_{\text{rms}}$.

Another type of electrostatic probes reported in [13, 36] employ electric potential variable capacitors known as varactors to detect the change in the induced electric field to determine the amount of variation in the voltage. As the probe circuitry requires ground connection, it should be located in a safe distance from the source of voltage and therefore exact distance from the surroundings determines the calculated capacitive couplings which affect the measurement.

2.1.4 Wireless Capacitive Sensor for Medium/High Voltage Measurement

The sensor reported in [11,12] is an active wireless voltage measurement device. This sensor measures the root mean square (RMS) of the voltage by connecting to a medium/high voltage conductor and harvesting the energy of the AC electric field surrounding the conductor. The authors introduce a moving average algorithm to self-calibrate the sensor and convert the measured current to the inducing voltage on the medium/high voltage. A matrix of the distances of the sensor to the surrounding objects is derived in order to calibrate the sensor in different configurations of one or three phase systems and variable distances to the ground. The information on the sensor is transmitted through a radio frequency an-

tenna to a receiver which collects the data. The recorded data is then analyzed using a computer. This type of sensor is only applicable in voltage measurement. The accuracy of the measured results for measurements conducted up to 35 kV is reported as ±5%.

2.1.5 Harmonics and Intermodulation Sensors

Another group of passive wireless sensors are the harmonics and intermodulation sensors. The harmonic sensors re-emit a harmonic of the interrogation signal, greatly reducing interference of the transmitting and receiving RF signals [37–39]. In the intermodulation method, the sensor is actuated by two signals with close frequencies and the response is a signal with the intermodulated frequency [40–42]. A longer interrogation distance is achievable using these methods as the difference between the transmitting and receiving frequencies causes a reduction in interference. The proximity of the transmitted and received signal frequencies in the intermodulation method compared to the harmonics method facilitates the circuit design and the compliance with the wireless carrier frequency bands. However, this advantage comes at a cost of lower conversion efficiency (30 dB loss as reported in [41]) with regards to the re-transmitted signal.

2.2 Wireless Interrogation of Passive Resonator-based Sensors

Passive wireless sensors are emerging to solve measurement problems where wires or fiber have disadvantages. The interrogation of the passive sensors are performed by remote methods depending on the type of sensor. These sensors are used for structural health monitoring [43, 44], medical [45–47], and industrial applications [48–50]. Interrogation of these sensors is done through coupling coils or antennas.

Most of the above mentioned sensors are employed in measuring almost stationary mea-

surements. Therefore, the time required for interrogation and analysis is not an important factor in the design of the interrogation systems. Typically, in order to increase the accuracy of the interrogation, a few samples of the almost stationary measurand is captured, hence increasing the time required to analyze one sample of the measurement. These methods are not adaptable to measure time variable measurands. A few of these interrogation methods are discussed in the following sections.

2.2.1 Capacitive/Inductive Coupling Interrogation

The coupled coil configuration is employed in short-distance interrogation with resonators of lower quality factor [45,50] to determine the resonance frequency or impedance variation of the sensor. The frequency range of these sensors is in the low to high frequency (LF to HF) bands, whereas the antennas are used for longer distances and higher quality factor resonators, operating in the GHz frequency range [43, 44, 51]. The former type of sensors have a simple, small structure which is desirable, however the interrogation distance is short as the received power from the sensor drops by $\frac{1}{R^6}$ (for the interrogation distance of R) [52–56]. The longer interrogation distances of the latter type of sensors is however facilitated by the advancements in the high frequency electronics [57].

2.2.2 Remote Wireless Interrogation Using Antennas

The proposed interrogation method in [43, 44, 58] for the measurement of mechanical strain is based on sending pulses of RF signals and analyzing the ringback of the resonator. The frequency of each pulse is determined by the previously recorded signals by the detector using a peak detection algorithm. The process takes a few seconds which is acceptable for strain measurement.

The airflow sensor in [48] is interrogated using a network analyzer and two antennas to derive the power difference between the RF input and the output (S_{12} parameter) of

the sensor. The minimum interrogation sampling time step in this case is dictated by the settling time of the network analyzer (typically 0.5 s).

Frequency counting is proposed in [57] as a resonance frequency detection method. This method can capture fast changes of the resonance frequency in the range of milliseconds by direct connection to the resonator and analyzing the changes in the voltage or current.

2.3 Proposed Passive Wireless Electric-Field Sensor and Wireless Interrogation

The proposed electric field sensor is a resonator with variable resonance frequency as a function of the surrounding AC electric field. The sensor is passive meaning it does not require change of batteries and it is interrogated wirelessly. Since the measurand is the time variable AC electric field, none of the previously proposed interrogation methods are applicable for the interrogation of the proposed electric field sensor. Hence, a new interrogation method is proposed. The proposed method is a remotely located interrogation system which sends pulses of radio frequency with a MHz repetition rate to the sensor and records the ring back of the resonator. The resonance frequency variation is determined by analyzing the ring back and then the corresponding electric field is determined. Electric field variations in the range of ms (potentialy μs) is measurable by this interrogation method.

None of the sensors discussed in this chapter, employed for the measurement of the electric field in the vicinity of high voltage apparatus, are passive and wireless. Unlike available resonator-based sensors, the proposed sensor/interrogation system is capable of measuring time-varying (non stationary) measurands. Further, the available passive wireless electric field sensors are generally used in short distance measurements whereas the proposed approach employs antennas and can achieve a longer interrogation distance.

The proposed method has the following advantages for the measurement of the electric

field in the vicinity of high voltage apparatus:

- The sensor is passive thus there is no need for batteries.
- Interrogation is done wirelessly from a safe distance.
- No grounding is required thus the risk of flash-over is reduced.
- Interrogation has a fast sampling rate which is capable of measuring variations in ms (potentially μs) range.
- Sensors are light and inexpensive potentially capable of distributed electric field/voltage measurement along a transmission line.

Further, the proposed interrogation method has the potential of extending the interrogation distance and simultaneous measurement of multiple sensors.

Chapter 3

Design and Fabrication of the Proposed Electric-Field Resonator Sensor

Design and fabrication of the proposed passive electric field sensor is discussed in this chapter. The sensor is composed of a coaxial cavity resonator with variable resonance frequency that is a function of the external electric field. The resonance frequency of the sensor is determined by wirelessly transmitted radio frequency pulses from an interrogator and analyzing the received damped sine wave which is referred to as the ring back of the resonator as shown in Fig. 3.1.

Resonator-based sensor structures and their pros and cons are discussed in this chapter. Then, finite element simulation results are presented which are used for maximizing specific characteristics of the sensor as a function of the sensor dimensions. The fabrication procedure using the simulation results is demonstrated in this chapter.

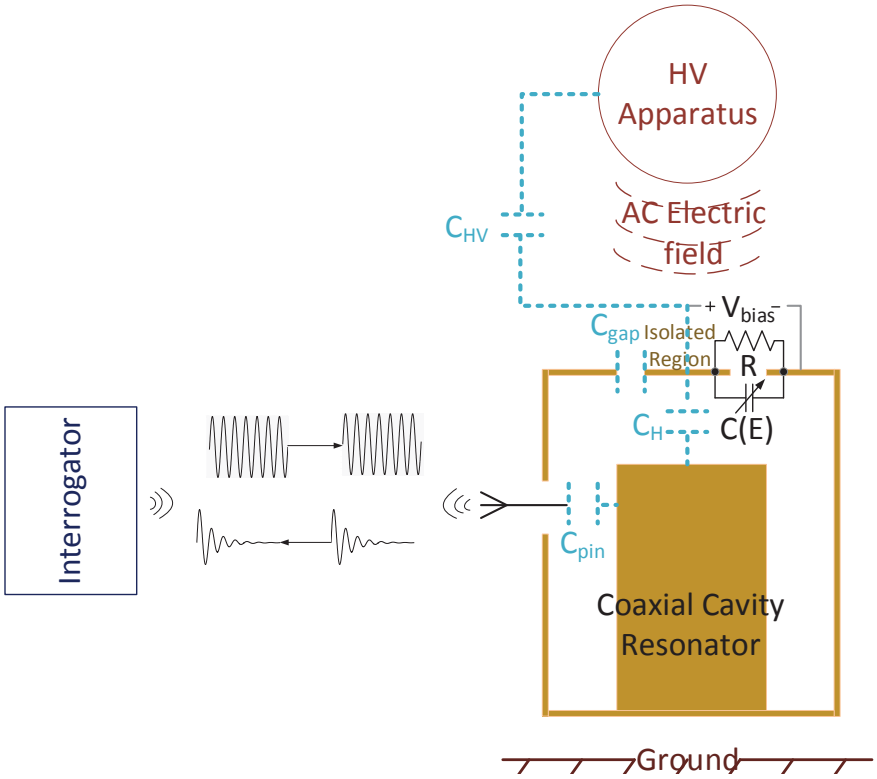

Fig. 3.1: A schematic of the coaxial cavity resonator capacitively coupled to a varactor as the sensor located in an external AC electric field and remotely interrogated . The interrogator transmits pulses of RF sine wave and receives the resonator ring back. The capacitors shown with the dotted lines are the circuit model of the resonator capacitive coupling.

3.1 Sensor Design

A resonator-based structure is chosen for designing the AC electric-field sensor in order to build a passive sensor with continuous-time interrogation. The sensor is designed based on a resonator that is capacitively coupled to varactors. Varactors are voltage-dependent, variable capacitance diodes in reverse bias. The electric field surrounding the sensor induces a voltage over the terminals of the varactor causing a shift in its capacitance which in turn changes the resonance frequency of the resonator/sensor.

3.1.1 Potential Resonator Structures

The important specifications in designing the resonator sensor are the frequency band, the range of change of the resonance frequency, and the quality factor of the resonator. The ISM band of 2.4GHz to 2.5GHz is chosen due to the size of the resonators and the reasonable price of the RF elements in this band. Since the shift in the resonance frequency is monitored, the range of change must be limited to the ISM band and a wider range of change would facilitate the detection of the shift in the resonance frequency. A higher quality factor will also increase the accuracy of the measured resonance frequency because of the method used for the interrogation which is discussed in detail in chapter 4. The sensor is designed to measure an AC, 60 Hz, electric field.

In this thesis, two resonator structures were implemented to study the properties of potential sensor structures. The first structure was a ring resonator etched on a coplanar waveguide (CPW) with varactors soldered over the ring as shown in Fig. 3.2.a. This type of resonator is proposed as a RF filter in [59]. The advantages of this structure are:

- The resonator shows a high range of resonance frequency variation by changing the varactors' capacitance.
- It has a robust structure making it suitable for mass production.

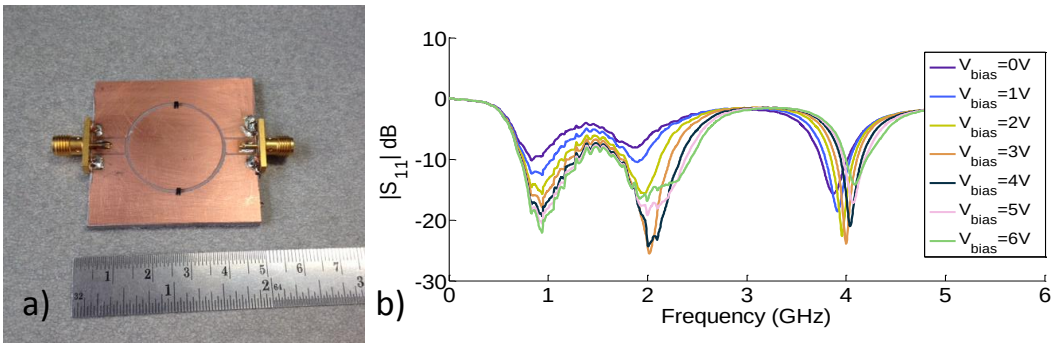

Fig. 3.2: a) Ring resonator capacitively coupled to varactors, and b) S_{11} measurement results at one port of the ring resonator with direct reverse bias voltage applied to the varactors.

The S_{11} measurement results in Fig. 3.2.b shows $\simeq$ 20 MHz of resonance frequency variation for 0 V to 6 V shift in reverse bias voltage of the varactors around 2 GHz resonance frequency. However, these resonators employed as RF sensors have the following disadvatages:

- Low quality factor ($\simeq 20$) and high loss.
- They are susceptible to noise interference.

A quarter-wave coaxial cavity resonator was also implemented with two SMA ports (shown in Fig. 3.3). One port is terminated by a varactor and the other one is used for interrogation. This type of resonator has the following advantages when used as a resonator-based sensor:

- Higher quality factor (≥ 500) and lower loss in comparison to a resonator etched on a printed circuit board (PCB).
- An acceptable resonance frequency variation as a function of the reverse bias voltage applied to the terminals of the varactors.

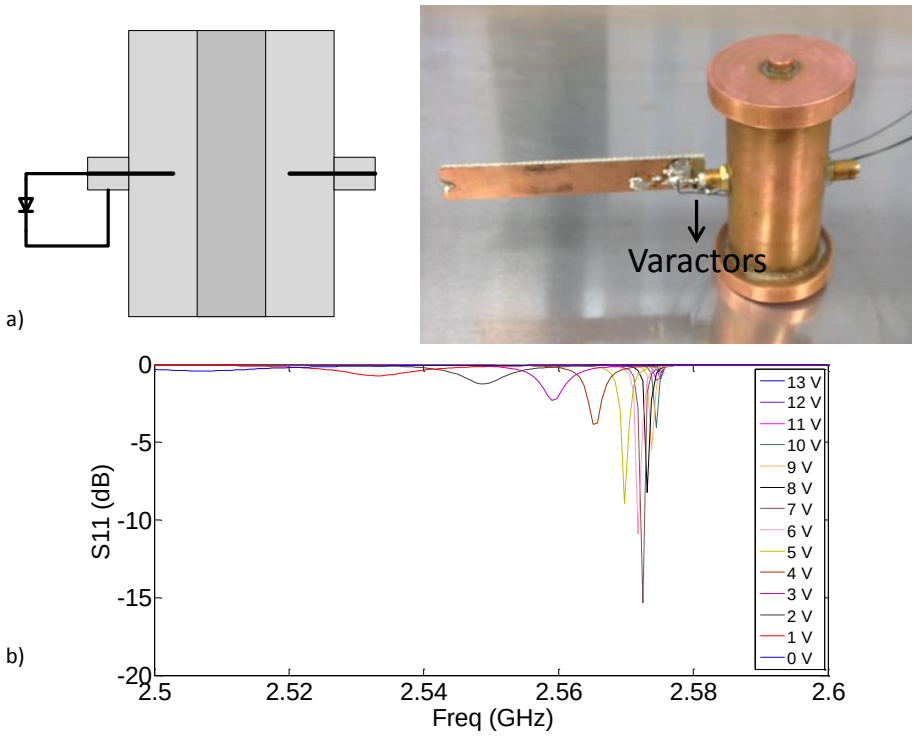

Fig. 3.3: a) Schematic and picture of a half wave coaxial cavity resonator with two SMA ports that is terminated by a varactor at one port, and b) S_{11} measurement results at the other port of the resonator with direct reverse bias voltage applied to the varactors.

However, a robust connection of the varactors to the SMA pin was not achievable. The varactors required close electrical conection to the SMA port for acceptable coupling to the coaxial resonator. Direct soldering of the varactors to the SMA is not feasible due to the uneven surface and the deformation of the SMA inner isolator caused by the heat applied during soldering. Therefore, a sensor structure composed of a coaxial cavity resonator with a robust varactor connection as discussed in the following section is proposed.

3.1.2 Proposed Sensor Design

The proposed sensor structure is composed of a radio frequency transmission line coaxial cavity resonator that is capacitively coupled to varactors inside the cavity. At the top of the sensor, an isolated region is formed on a printed circuit board (PCB) and the varators bridge across the gap between this isolated region and the surrounding conductor. The coaxial transmission line ($Z_0 \simeq 90\Omega$) cavity resonator is capcitively coupled to this isolated region and hence to the varactors. An external AC electric field is also capacitively coupled to this isolated region inducing a potential across the varactors. The electrical isolation of the isolated region is required for the creation of the reverse bias voltage induced by the surrounding AC electric field. The isolated region forms a parasitic capacitance that is in parallel to the varactor ($C_{gap} \simeq 0.25$ pF) and the capacitive load of the air gap ($C_H \simeq 0.25$ pF). The variation of the external AC electric field will change the capacitance of the varactors ($C(E) \simeq 0.683$ pF $- 2.35$ pF), which in turn changes the capacitive loading seen by the resonator and consequently its resonance frequency.

The perturbation in the varactor capacitive loading at one end of the coaxial transmission line results in a shift in the resonance frequency measured at the antenna port. A capacitive coupling (C_{pin}) couples the RF signal from the antenna to the resonator and from the resonator to the antenna. A simplified equivalent circuit model of the sensor is shown in Fig. 3.4. The demonstration of the equivalent circuit helps with understanding the overall effect of each parameter in the design. The capacitive values in the equivalent circuit are highly sensitive to the resonator dimensions. Therefore, an accurate 3D model of the sensor is simulated using finite element analysis to derive the design parameters.

In the schematic structure of the sensor shown in Fig. 3.5, two varactors with reverse polarities must be placed in series in order to capture both positive and negative half cycles of the external AC electric field. In each cycle, one varactor will be reversely biased and the other one will be conducting. Each varactor will also require a conducting path for the

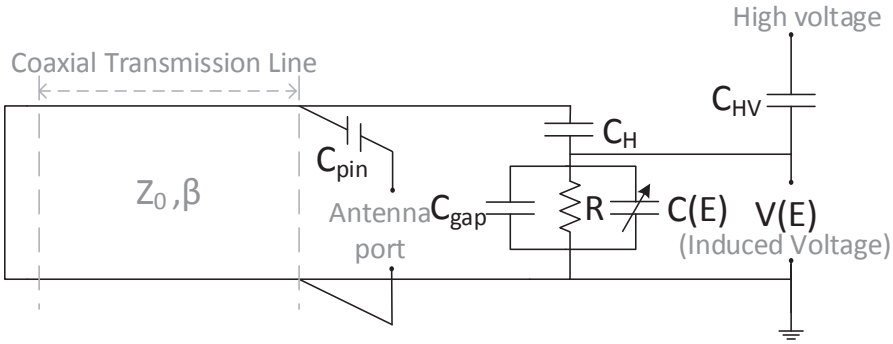

Fig. 3.4: The equivalent circuit model of the coaxial cavity resonator consisting of a TEM mode coaxial transmission line short circuited at one end and capacitively loaded at the other. The potential over the varactor is capacitively induced by the high voltage.

accumulated charges on the varactor capacitance in each cycle to be discharged in the next cycle. This path will be provided by the resistors placed in parallel with each varactor.

3.2 Sensor Fabrication

The fabrication procedure of the proposed sensor structure as a coaxial transmission line loaded with varactors is discussed in this section. The key features in successful interrogation of the electric field sensor are introduced. Later, the influence of the resonator dimensions on these features are studied by simulation and measurement results.

3.2.1 Key Features in Sensor Fabrication

Two of the key features in designing the interrogation system are the interrogation distance and accuracy that are controlled by the quality factor of the resonator. Increasing the quality factor of the resonator will increase the resonance frequency discrimination of the measured ring backs. Higher quality factor decreases the damping, which lengthens the exponentially-decaying sine wave at the ring back and reduces the uncertainty of the measured resonance frequency. Therefore, low loss materials are used to fabricate the cavity. As the timing of

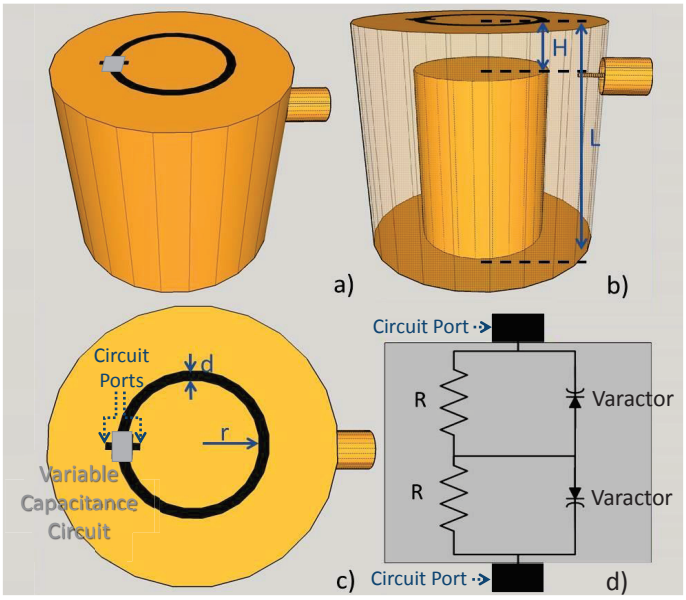

Fig. 3.5: Sensor structure: a) External side view, b) Internal side view, c) Top view and d) Details of the variable capacitance circuit shown in part c.

the peaks is used for determining the frequency of the ring back signals by the interrogator, a larger number of detectable peaks will decrease the uncertainty of the detected resonance frequency. A coaxial transmission line cavity resonator is chosen in this design for its high quality factor compared to those fabricated with PCBs. In the sensor structure shown in Fig. 3.5, the main factors in determining the quality factor are the dimensions of the resonator and the radius of the isolated region. The sensitivity of the resonance frequency f_r to the applied electric field E_{AC} is defined as $\Delta f_r/\Delta E_{AC}$ which should also be maximized. This parameter shows the maximum resonance frequency shifting with respect to the changes in the electric field. The sensitivity is largely determined by the rate of change of capacitance with the maximum electric potential that can be applied over the terminals of the varactor.

The dimensions of the cavity resonator and the isolation ring on the top loading PCB were designed to keep the resonance frequency in the ISM band (2400 MHz to 2500 MHz) and also achieve the above mentioned properties, *i.e.* higher quality factor and higher

sensitivity. This ISM band was chosen because the frequency range is high enough to utilize small antennas and with a large selection of commercially available options.

3.2.2 Selected Fabrication Features

Some of the structure features of the sensor have been chosen with fixed dimensions and the rest were chosen using finite element simulation results. The fixed features were the type of varactor and the radii of the inner and the outer coaxial transmission line. SMV1231 from Skyworks was chosen as the varactor for its low resistive loss. The inner and outer radii of the coaxial transmission line were chosen based on the standard dimensions of available copper pipes. The outer cylinder has a radius of 14.29 mm on the inside and the inner cylinder has an outside radius of 7.94 mm (standard 1.125″ and 0.5″ copper pipes).

An SMA connector is threaded through the wall and the signal on the center conductor capacitively couples the received energy from the antenna into the resonator during the transmitting cycle of the interrogation. It also transfers the energy from the cavity to the antenna when the RF pulse has been switched off and the energy from the cavity is being re-emitted (see Fig. 3.1). The effects of the depth of the SMA pin inside the resonator, and hence the capacitive coupling, is studied in [58]. The overall quality factor decreases with deeper SMA pin placement while the energy coupling increases. Increased coupling will decrease the loaded quality factor of the resonator as the loading effect increases. The desired depth of the SMA pin connector was determined by analyzing the S_{11} measurement results and setting the S_{11} to -8 dB. This setting was found to be a reasonable trade off between the re-emitting signal levels and the cavity loss.

The ring gap surrounding the isolated region is milled on a PCB (Rogers, RT/duroid 6002 with copper cladding of 35 μm chosen for its low loss and low thermal coefficient of +12 ppm/°C). The varactors are installed on the isolated region gap in parallel with resistors that provide the discharge path. SMD thick film resistors with a value of 475 MΩ

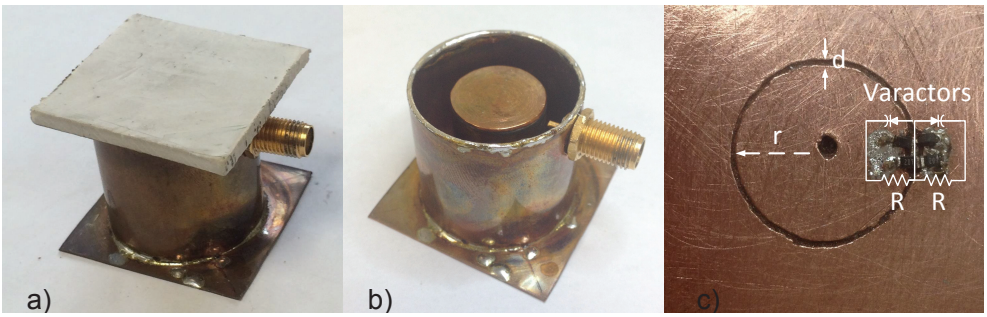

Fig. 3.6: Resonator structure: a) external side view, b) inside view with the top PCB removed, and c) top PCB plate with the varactors and resistors.

were used for this design. As will be shown later, the value of R determines the dynamic range.

The gap distance, H, significantly affects the shift in resonance frequency and the quality factor. Therefore, three resonators were made with similar top PCBs with H = 3, 4, and 5 mm to measure the variation of the resonator parameters caused by H. The length of the outer cylinder (L) was chosen such that the resonance frequency of the cavity will remain in the specified ISM band. The resonators were built with r + d = 7 mm and d = 1 mm in order to increase the resonance frequency shift which will be verified by simulation in the following section (see Table 3.1).

The maximum frequency shift reported in Table 3.1 is derived from direct application of a DC voltage (0 V to 5 V) over the varactor terminals of the resonator and measuring the S_{11} parameter using a network analyzer. The quality factor is derived by analyzing the recorded ring-down of the re-emitted signal using (4.1) discussed in the following section. From Table 3.1, a conclusion can be made that there is a trade off between the frequency shift and the quality factor when H varies.

The frequency shift reported in Table 3.1 has been derived from S_{11} measurement of the cavity resonator using a network analyzer. A direct DC voltage was applied to the terminals of the varactors and S_{11} was measured using a network analyzer. The variation

Table 3.1: Measured quality factor and maximum resonance frequency shift for three different L and H with fixed values of $r = 6\ mm$, $d = 1\ mm$ and $R = 475\ \mathrm{M}\Omega$.

L (mm)	H (mm)	f_r (GHz) at $V_{Bias} = 0$ (V)	Δf_r (MHz) for $V_{Bias} = 0 - 5$ (V)	Quality factor
29.5	5	2.449	11	462
28.0	4	2.404	13	240
25.5	3	2.413	19	100

of the measured S_{11} of the resonator with L = 29.5 mm, H = 5 mm, r = 6 mm, and d = 1 mm as a function of the bias voltage is shown in Fig. 3.7. The results of the S-parameter measurements represent the sensitivity of the sensor to the voltage variation which is linearly related to the electric field variation. The resonance frequency shifts by 9 MHz for a bias voltage variation of 0 V to 5 V.

3.2.3 Maximizing Selected Features Using FEM Simulation Results

A finite element simulation (FEM) of the resonator loaded with a lumped capacitor representing the reverse biased varactor was performed in COMSOL software in order to determine best values of r and d such that the shift in the resonance frequency increases for a given change in the varactor capacitance. A 3D model of the sensor with the SMA port was implemented in COMSOL as shown in Fig. 3.8.

In the simulation, Comsol RF module is used to measure the resonance frequency of the sensor. The SMA on the side of the sensor is defined as a port to measure the S_{11}. The meshing of the cavity is chosen on the fine setting of the simulator, hence the mesh size surrounding the SMA pin and the top PCB are more dense (*i.e.* minimum 0.3 mm and maximum 2.4 mm).

The 3D model was then transferred to MATLAB software using the software package COMSOL with MATLAB. The software generates a MATLAB code of the model which

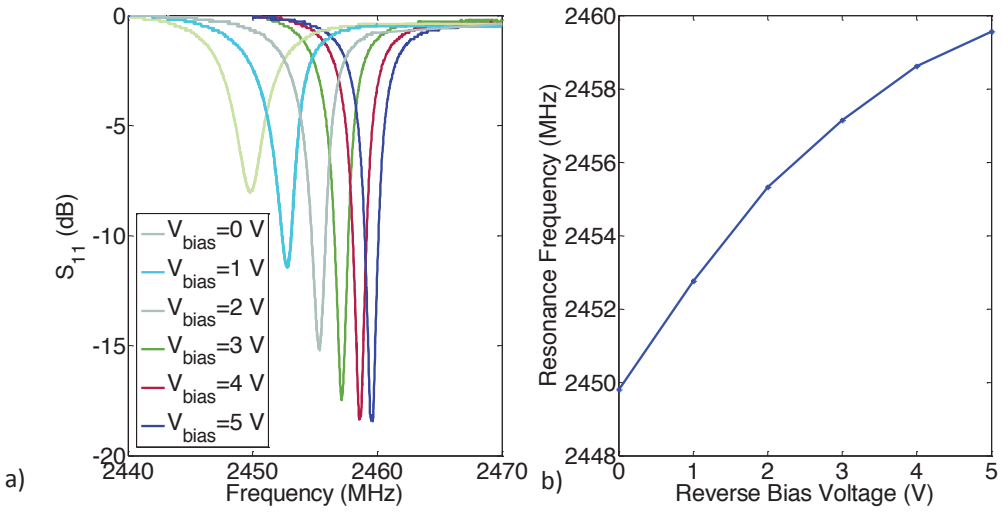

Fig. 3.7: S-parameter measurement results; a) S_{11} vs. frequency with L=29.5 mm, H=5 mm, r=6 mm, and d=1 mm for different DC reverse bias voltages, b) resonance frequency shift caused by a direct DC reverse bias voltage applied to the terminals of the varactor.

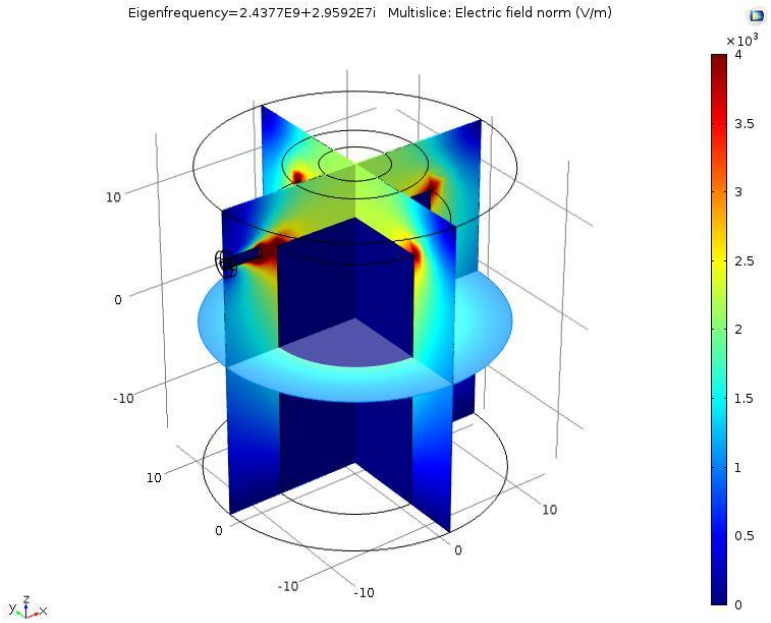

Fig. 3.8: 3D implementation of the sensor in COMSOL FEM simulation software. The sensor is shown in RF resonance mode.

is executable in MATLAB. The software package is used to run the COMSOL simulation multiple times in a MATLAB function. The resonance frequency is determined by varying the input RF frequency and determining the minimum S_{11} using genetic algorithm. Since running the generated code for a complete frequency sweep is time consuming, genetic algorithm tool in MATLAB is used in determining the frequency at the point that S_{11} is minimum. Determining the S_{11} value at each frequency for a 3D model takes more than 10 minutes. In the case of a complete frequency sweep for determining the exact frequency at which S_{11} is minimized, the simulation has to be repeated numerous times. The complete frequency sweep will take days to be simulated. Therefore, genetic algorithm is employed to find the frequency at minimum S_{11} amplitude by evaluating some frequency points. Using genetic algorithm, the simulation time is reduced to one hour. Then, the maximum shift in the resonance frequency is determined for a given change in the varactor capacitance. The SMV1231 capacitance-voltage characteristics in the range of 0 V to 5 V of the reverse bias voltage shows a wide range of variation in the capacitance value, *i.e.* 2.35 pF to 0.683 pF.

Assuming L = 29.5 mm and H = 5 mm, which were selected for a high quality factor from Table 3.1, the variation of the resonance frequency as a function of the ring radius surrounding the isolated region is shown in Fig 3.9. The simulation results indicate that a smaller isolated region gap will result in a bigger resonance frequency shift. Further, the frequency variation is maximized for a specific isolation ring radius when the outer radius of the ring r + d equals the inside cylinder outer body radius of 7.94 mm. The dimensions r = 6 mm and d = 1 mm of the resonator built in this work are identified in Fig. 3.9. This operating point is not chosen exactly at the maximum of Fig. 3.9 to avoid getting into the sharp dropping point on the graph by slight variation of r in the fabrication procedure of the resonator. The parameters chosen for the final design are listed in Table 3.2.

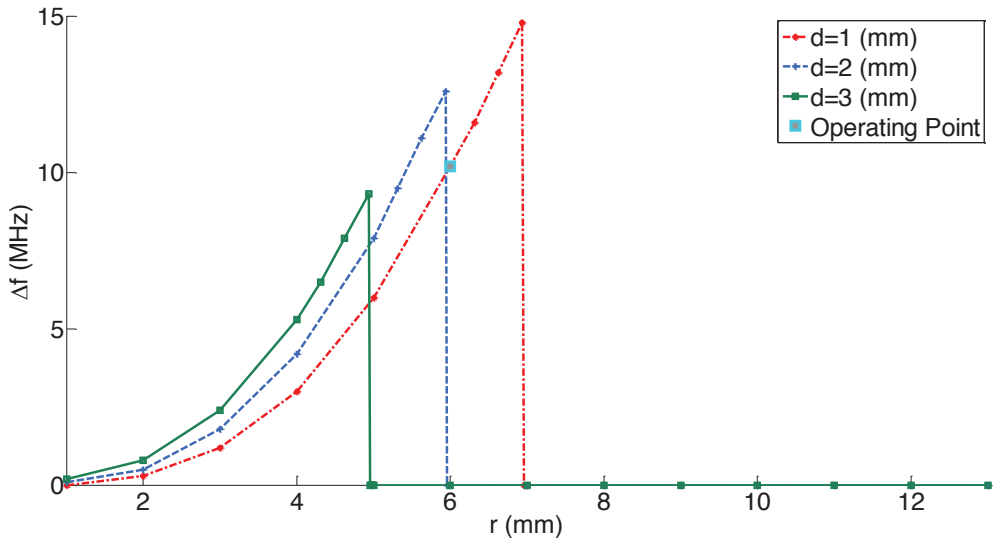

Fig. 3.9: Maximum shift in resonance frequency versus the isolated region radius (r) for different isolated region gap (d), (see Fig. 3.6), assuming a reverse bias voltage in the range of 0 V to 5 V and a resonator with L $= 29.5$ mm and H $= 5$ mm.

Table 3.2: List of parameters and dimensions chosen for the final design. The parameter labels are shown in Fig. 3.5.

Parameters	Dimensions/Type
L (mm)	29.5
H (mm)	5
d (mm)	1
r (mm)	6
R (MΩ)	475
Varactor (type)	SMV1231

3.3 Summary

In this chapter, the design and fabrication procedure of the sensor is discussed. The sensor is composed of a coaxial cavity resonator capacitively coupled to varactors. The resonance frequency of the cavity (in the TEM mode) varies by the changes in the capacitance of the varactors. The sensor is fabricated using copper tubes and an SMA connector on the side of the cavity is employed to couple the energy into and outside of the resonator.

The sensor is designed to resonate in the frequency band of 2.4 GHz to 2.5 GHz dictated by the ISM band regulations. Important features for successful interrogation are higher quality factor of the resonator and a larger shift in the resonance frequency corresponding to the change in the varactor's capacitance. The effect of the dimensions of the sensor on these features were analyzed using finite element method simulation results.

Chapter 4

Interrogation System Details

In this chapter, an interrogation system compatible with the sensor which facilitates a high sampling rate of the AC electric field is proposed and discussed. The interrogation system transmits pulses of RF signal and records the damped sine waves (the so-called ring backs) re-emitted from the sensor. The instantaneous AC electric field is then determined by deriving the frequency of each ring back. The timing and frequency analysis of the interrogation method is also discussed. Later, the measurement results are reported and the interrogation distance is analyzed using the radar equation. The interrogation method is comparable to radar systems as the sensor is passive and similar to a reflector.

4.1 Interrogation Setup

Measurement of an AC electric field requires determination of the resonance frequency several times in each period of the AC electric field. For example, for a high voltage device operating at 50/60 Hz with a period of 20/16.67 ms at least 10 samples per cycle are required, corresponding to a minimum interrogation sampling frequency of 500/600 samples/s. Higher AC field frequencies require higher sampling rates.

The majority of the existing wireless interrogation systems are designed to measure

almost stationary measurands [43, 44, 48, 58]. The approach that is chosen in this thesis to measure the time-varying measurand is based on analyzing the down converted RF pulses received from the sensor. This approach requires major signal processing on signals recorded by high resolution measuring devices (i.e. a high frequency oscilloscope). Other approaches have been reported in measuring time varying measurands in the range of milliseconds [57]. These methods mainly focus on the design of the interrogation circuitry while the main focus in this thesis is on improving the processing techniques applied to the received signal in order to reduce the effect of noise and interference and increase the interrogation distance.

The procedure of mapping each resonance frequency to the corresponding electric field is illustrated in Fig. 4.1. In order to estimate the electric field strength surrounding the sensor, the resonance frequency of the sensor/resonator versus time is measured as shown in Fig. 4.1.a. By mapping this resonance frequency to the corresponding reverse bias voltage over the varactors, bias voltage is determined which can then be mapped to the inducing electric field. The graph in Fig. 4.1.b, which shows the variation of the resonance frequency versus the reverse bias voltage of the varactor, is derived using S-parameter measurement of the resonator and Fig. 4.1.c is derived using finite element simulation. The electric field at the sensor location around the high voltage apparatus is calculated using finite element simulation of the high voltage apparatus over the ground. Figure 4.1.d shows the absolute value of the electric field sampled in time. The varactor's characteristic capacitance determines the variation of the resonance frequency by the reverse bias voltage as shown in Fig. 4.1b.

A block diagram of this interrogation setup is shown in Fig. 4.2 (Details in Appendix A). In this setup, an RF signal is switched on to energize the sensor and is turned off when receiving the ring back. The frequency of the RF signal is set to a value close to the resonance frequency of the resonator (discussed in section 4.2). The frequency of switching determines the rate at which the ring back of the sensor is recorded and the repetition of

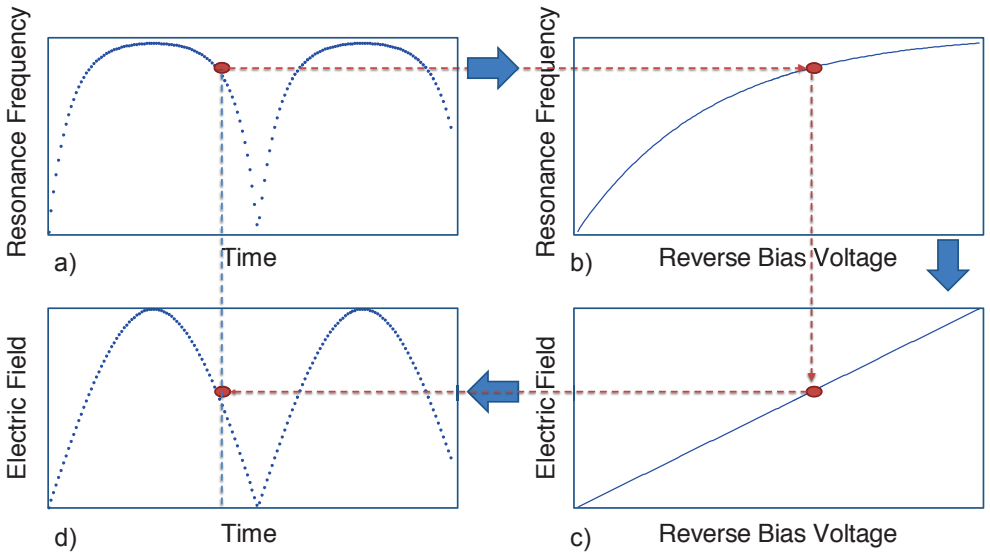

Fig. 4.1: Mapping the shift in resonance frequency to the corresponding electric field amplitude: a) measured resonance frequency vs. time, b) resonance frequency vs. reverse bias voltage derived using S-parameter measurement, c) electric field amplitude vs. reverse bias voltage calculated using finite element simulation and d) the final result: absolute value of the electric field vs. time.

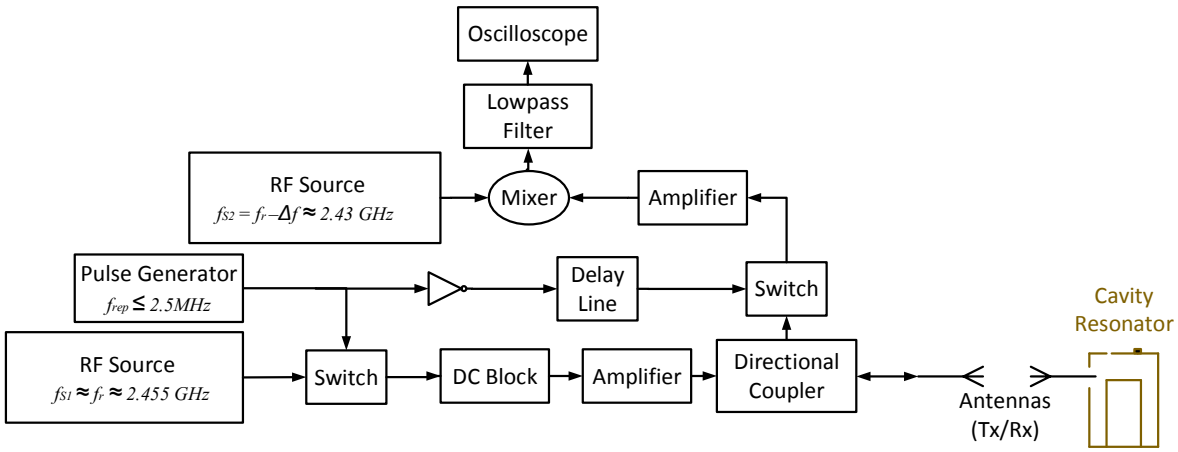

Fig. 4.2: A block diagram of the interrogation setup.

electric field that is measured. During the on time of the switch, the RF power is coupled to the resonator through the antenna. When the switch is turned off, the sensor resonates at its natural frequency and emits an RF signal at this frequency. The ring back of the resonator is received by the interrogator antenna and is down converted by mixing with an RF signal (shown in Fig. 4.3) which is 20 MHz to 30 MHz lower than the transmitted frequency. This ring back is digitized using a fast sampling oscilloscope (Agilent DSO9254A).

The RF elements of the receiver between the antenna and the mixer consists of a

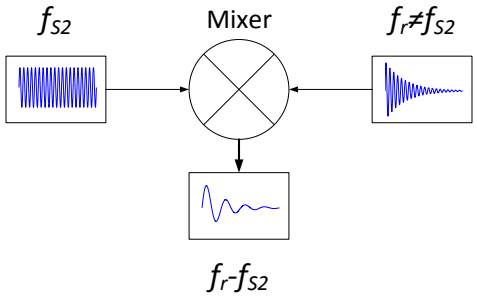

Fig. 4.3: A demonstration of the mixer operation.

directional coupler which separates the transmitted and received signals and a second switch which is used at the input of the receiver to stop the reflected pulses from the scattering objects in front of the interrogator antenna. The receiver will start capturing the signal with a defined delay after the transmitting signal is switched off. The delay is manually set to the approximate maximum time required for the pulses to travel to the farthest scattering object and reflect back, *e.g.* 60 ns for 10 m. By determining the time between peaks during the ring back, the resonance frequency of the sensor can be estimated. By mapping the resonance frequency estimates to the corresponding electric fields (as shown in Fig 4.1), the electric field variation in time is obtained.

The picture of the interrogation setup is shown in Fig. 4.4. The computer is used for setting the frequencies of the RF sources, and also analyzing the recorded data on the oscilloscope. The Pulse generator and the DC source provide the TTL (Transistor transistor logic) signal of the switches and the DC bias of the amplifiers. The output of the directional coupler is connected to the transceiver antenna which is not shown in this picture.

A few samples of RF pulses that are sent as input to the antenna of the interrogator are shown in Fig. 4.5 in addition to the switching TTL. The pulses have 2 MHz switching frequency, 100 ns duty cycle and 7 dBm power.

The results of the signals received at the output of the receiver antenna are recorded and shown in Fig. 4.6. In this study, a $3-$dB attenuator is used between the output of the coupler and the resonator replacing the wireless path loss. The attenuation resembles the wireless loss between the antennas. This method is employed to reduce the effect of non-thermal noises and reflections. The $3-$dB attenuation simulates a distance of 15 cm between the antennas. In Fig. 4.6, the received signal after the coupler (shown in Fig. 4.6.a) is the ring back of the resonator with -13 dBm power. The signal is then switched (shown in Fig. 4.6.b) to reduce the effect of reflected signals from the surrounding scattering objects as was mentioned in previous paragraphs. Since the scattering objects are in close

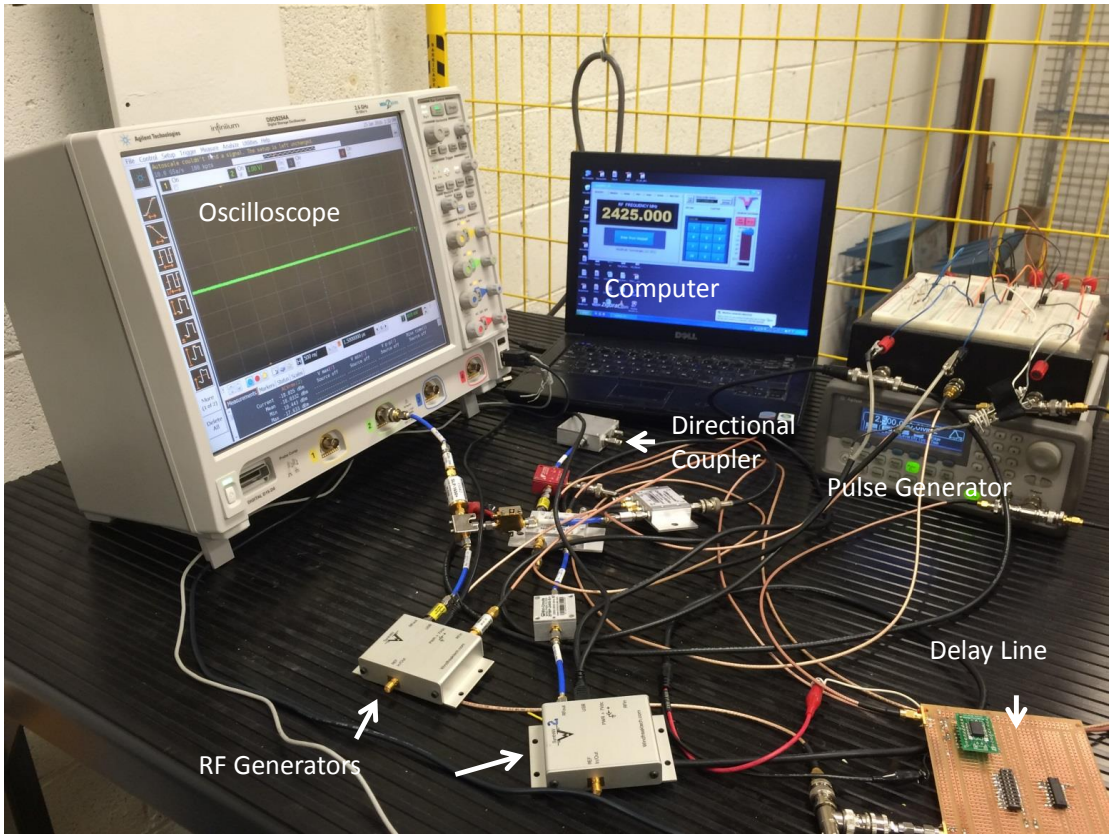

Fig. 4.4: A photo of the interrogation setup. The computer is controlling the frequency and power of the RF generators. The pulse generator and the delay line provide the TTL signal of the switches (TTL of the receiving switch is delayed comparing to the transmitting). The oscilloscope records the data. The output of the directional coupler is connected to the RX/TX antenna through coaxial cables.

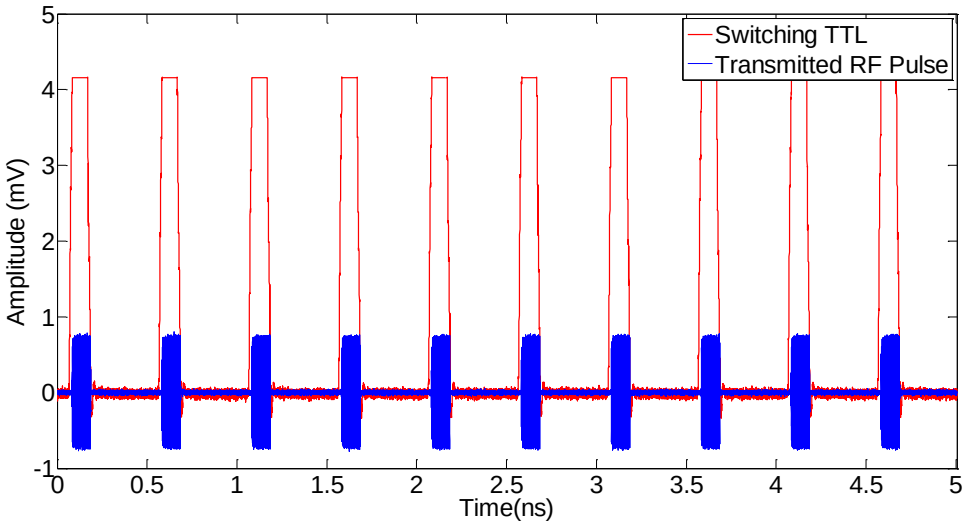

Fig. 4.5: A few samples of the transmitting pulse and the switching trigger.

distance to the senosr, the delay in the switching is set to 10 ns. The switched signal is then amplified (shown in Fig. 4.6.c) using a 10 dB amplifier. Then, the frequency of the ring back is down converted by mixing with a signal in 30 MHz difference from the resonance frequency. The output of the mixer after passing through a low pass filter is shown in Fig. 4.6.d. The low pass filter is used to reduce the high frequency noise and feedthrough of the RF signals. The power of the ring downs recorded by the oscilloscope are reduced to -10 dBm.

In order to determine the exact time of the peaks, signal processing techniques such as noise reduction and peak detection methods are applied. A sample of the measured ring down waveform is shown in Fig. 4.7 with the peak locations identified. Averaging over n number of the consecutive ring backs increases the SNR (Signal to Noise Ratio) by the $\sqrt{n}$. However, averaging will reduce the sampling number of interrogation by a factor of n which is negligible due to the fast initial interrogation sampling rate of 2 MHz employed for measuring a 60 Hz AC electric field. The averaged results are then filtered through a

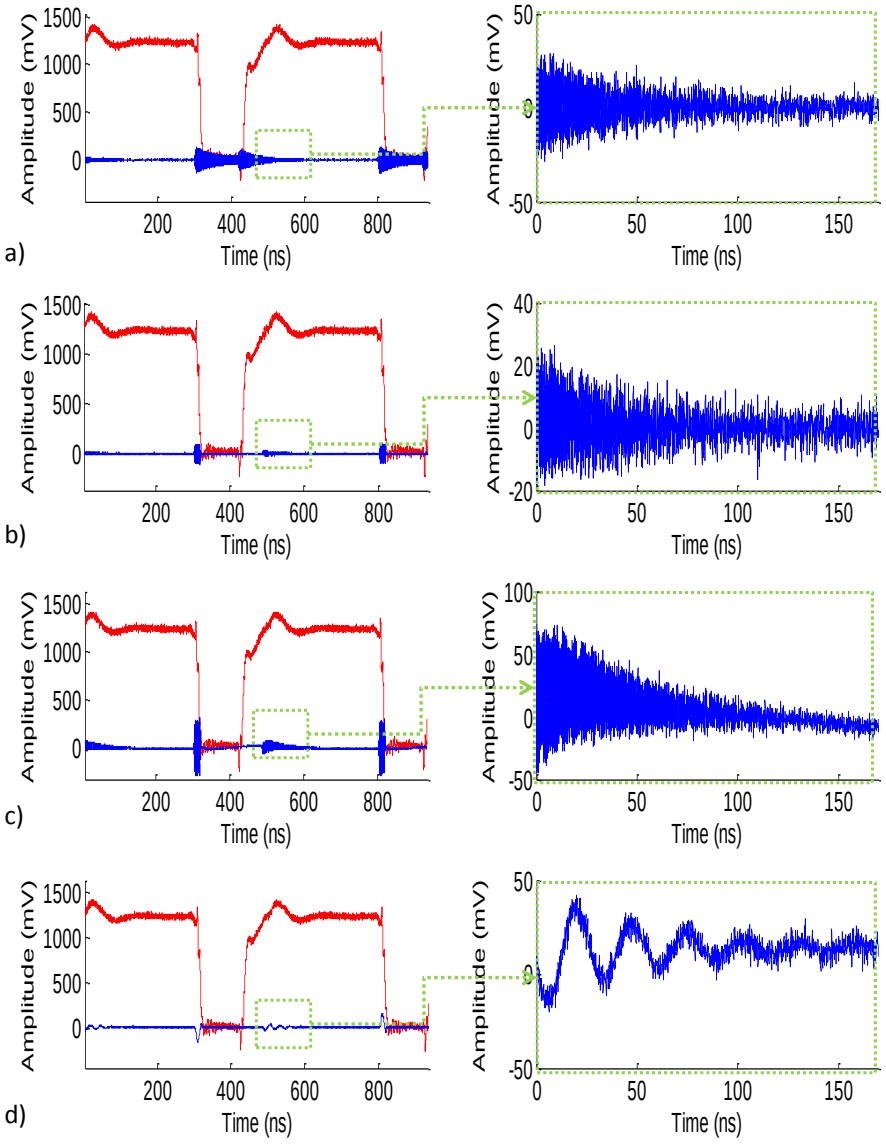

Fig. 4.6: The processing steps of the received ring backs in addition to the TTL of the switch. The graphs depict the signals and a zoom in on the ring backs as follows: a) output of the directional coupler, b) the signal after switching, c) the amplified signal, and d) after mixing with an RF signal with 30 MHz difference from the resonance frequency.

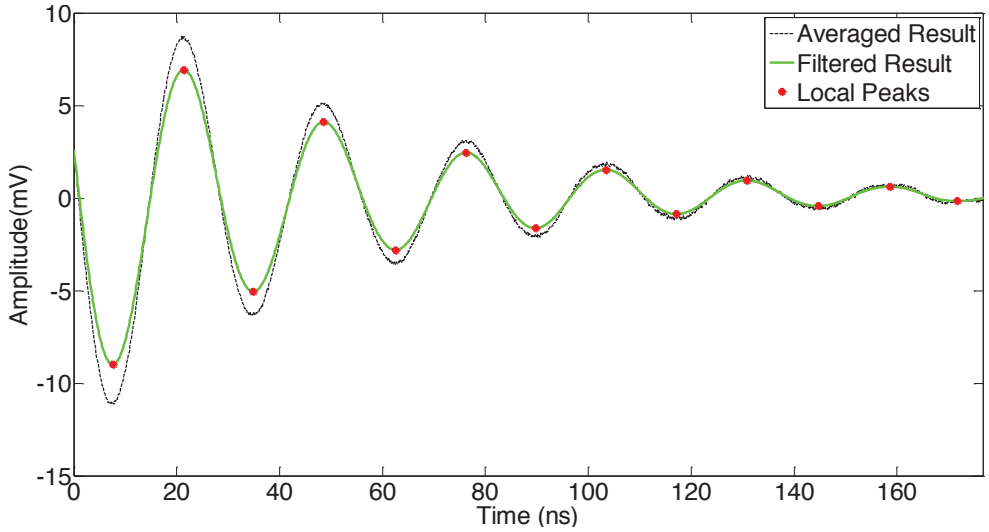

Fig. 4.7: Ring back recorded by the oscilloscope when the RF transmitter is turned off and the sensor is connected to the interrogation system through coaxial cables and a 3 dB attenuator. The resonator parameters are H=5 mm, L=29.5 mm, r=6 mm, d=1 mm, and R=475 MΩ. The averaged signal shown in this graph is for n= 50 (number of averaging).

low-pass filter to cancel the noise effect. Further, a peak detection technique is applied to the filtered signal to find the exact time of the peaks between the discrete samples recorded by the oscilloscope. The zero-crossing point of the derivative of the signal around the peaks gives an estimate of the exact time of the peaks. Further, the 10 Gsa/s sampling rate of the oscilloscope increases the accuracy of the estimated peak locations. Every time the RF signal is turned off, the resonance frequency measured from the ring back can be used to estimate the electric potential applied over the terminals of the varactor of the sensor at that time. The effects of the sampling rate, averaging, and SNR on the measurement results are further discussed in Section 4.5 using the measurement results.

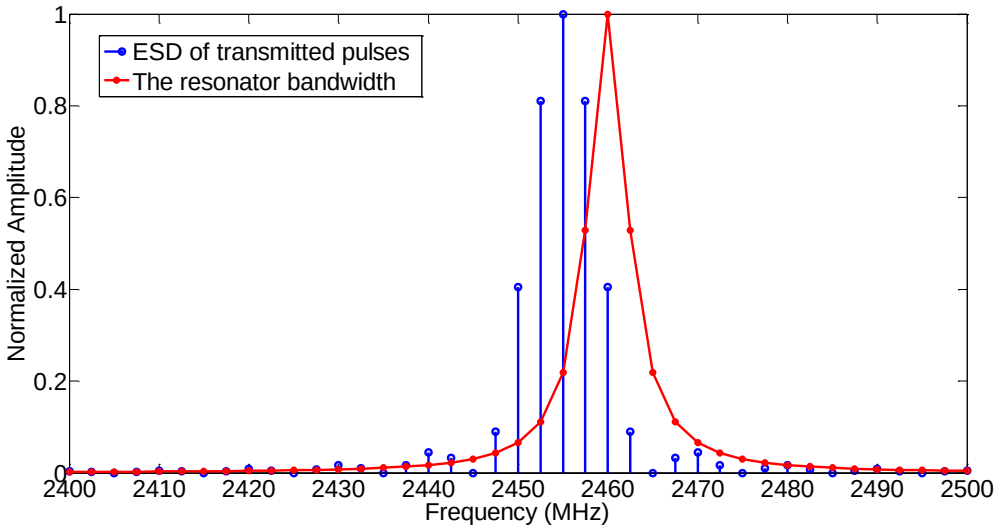

Fig. 4.8: An overlap of the energy spectral density (ESD) of the transmitted RF pulses and an approximation of the resonator bandwidth assuming $f_{rep} = 2.5$ MHz, $T_0 = 100$ ns, $f_{S1} = 2455$ MHz, and $f_r = 2460$ MHz.

4.2 Interrogation Frequency Spectrum Analysis

The normalized energy spectral density of the RF pulses transmitted by the interrogator is a train of impulses in the frequency domain with an envelope of a sinc function as shown in Fig. 4.8. The resonator is assumed to be an ideal filter with a bandwidth of $f_r/Q = 5.3$MHz. For the proposed interrogation method, the main lobe of the sinc function must have the maximum overlap with the resonator bandwidth.

The resonance frequency of the sensor varies in the range of 2450 MHz to 2460 MHz according to Fig. 3.7. Considering a bandwidth of 5.3 MHz for the resonator, the sinc function main lobe must approximately cover the range 2445 MHz to 2465 MHz. Therefore, the transmitted RF signal frequency is set to 2455 MHz to increase the coupling. The switching duty cycle (T_0) which determines the sinc function main lobe width is set to $T_0 = 1/10$ MHz $= 100$ ns.

The least amount of coupling is for the resonance frequencies of 2450 MHz or 2460 MHz

corresponding to a minimum of 34% energy absorption from the antenna and an approximate energy loss of $-4.7\,\mathrm{dB}$. The amount of energy loss is derived by integrating part of energy spectral density of the transmitted pulses that overlaps with the resonator bandwidth at the defined least coupling frequencies.

4.3 Interrogation Timing Analysis

The interrogator sends pulses of radio frequency signal with $\mathrm{f_{S1}} = 2455$ MHz to the resonator. From the ring back time (shown in Fig. 4.7), the loaded quality factor of the resonator including the antenna loading can be determined as

$$\mathrm{Q} = \tau\pi\mathrm{f_r} = (60\,\mathrm{ns}) \times \pi \times (2.449\,\mathrm{GHz}) = 462. \tag{4.1}$$

In this equation, τ is the ring back time constant (time required for the amplitude to drop by $\frac{1}{e}$) and Q is the quality factor. The value of $\tau = 60\,\mathrm{ns}$ represents the worst case scenario derived from the measurements.

Allowing $\mathrm{T_0} = 100\,ns = 1.7\tau$ for excitation and $5\tau = 300\,\mathrm{ns}$ for the resonator ring back to damp, the resonator is energized to 81.1% and de-energized to 99.3% of its initial energy. There is a $-0.9\,\mathrm{dB}$ loss due to the small energizing and de-energizing time in addition to $-4.7\,\mathrm{dB}$ loss caused by the spectrum overlap. The acceptable repetition rate must be close to or less than

$$\mathrm{f_{rep}} = \frac{1}{\mathrm{T_0} + 5\tau} = \frac{1}{100\,\mathrm{ns} + 5 \times 60\,\mathrm{ns}} = 2.5\,\mathrm{MHz}. \tag{4.2}$$

where τ is the ring back time constant and $\mathrm{f_{rep}}$ is the switching frequency of the interrogator. In order to reduce the noise effect, 50 consecutive samples are averaged, reducing the effective interrogation sampling rate to $\mathrm{f_{si}} = \mathrm{f_{rep}}/50 = 50$ kHz which is still much higher than the required sampling rate of 600 Hz for the measurement of an AC, 60 Hz electric field.

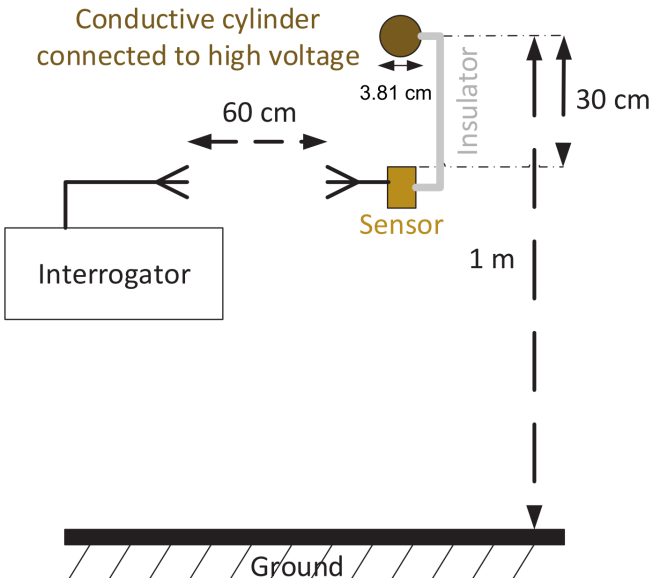

Fig. 4.9: Laboratory measurement setup for the measurement of the electric field below a cylindrical conductor above ground. The cylindrical conductor is energized by a 60-Hz, 1.7-kV_{rms} AC voltage.

4.4 Measurement Results

The measurement of an AC electric field was performed by locating the resonator under an energized cylindrical conductor over a large ground plane as shown in Fig. 4.9. The bottom plate of the resonator is parallel to the ground plane. The resonator is hanging from the conductor by an insulator, *i.e.* a piece of foam, and is not electrically connected to the ground. The interrogation distance of the antennas is 60 cm and the interrogation switching rate is $f_{rep} = 2.5$ MHz. The resonance frequency variation of the measurement in time is shown in Fig. 4.10.

In order to derive the electric field variation in time from Fig. 4.10, the mapping graphs shown in Fig 4.1.b and 4.1.c are employed. As the electric field and the bias voltage have a linear relation (Fig. 4.1.c), these two graphs are combined into one graph showing the electric field variation by the resonance frequency for simplicity. The relationship between

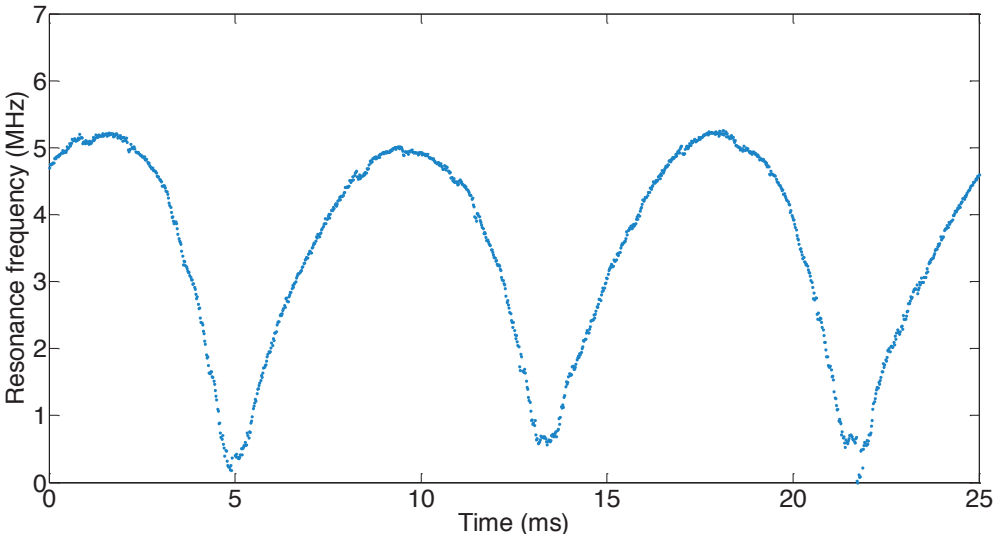

Fig. 4.10: Shift of resonance frequency vs time for a 60 Hz AC voltage when 1.7 kV_{rms} is applied to the cylindrical conductor.

the shift in the resonance frequency and the AC electric field is shown in Fig. 4.11. This graph is derived by applying known voltages and numerically-determined electric fields induced by the cylindrical conductor. In the numerical simulation (using finite elements method) the electric field has been determined at the location of the sensor's PCB in the absence of the sensor.

Using the graph of Fig. 4.11, the final result which is the electric field variation in time is derived and shown in Fig. 4.12. The inacuracy in the measured electric field near zero is a result of the resistor R= 475 MΩ causing a reduction in the discharging time of the varactor capacitance (C_{var}) to nearly $RC_{var} \simeq 1$ ms eliminating the sharp change around zero.

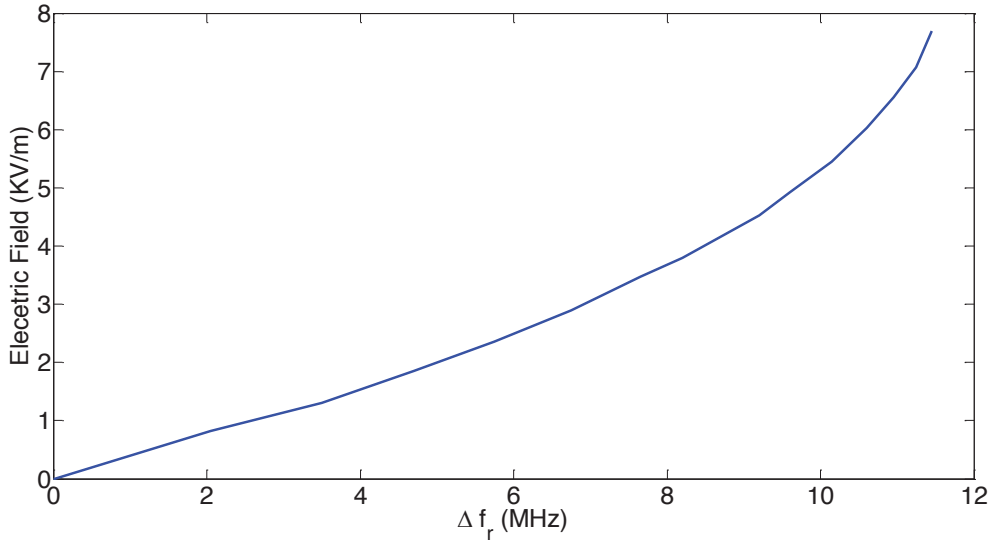

Fig. 4.11: Electric field vs. shift in the resonance frequency obtained by AC electric field measurements.

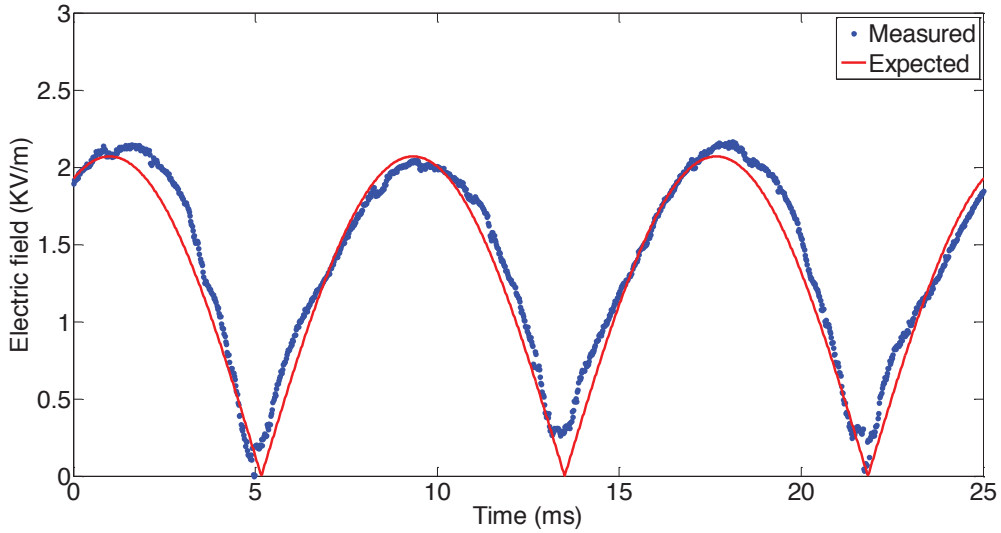

Fig. 4.12: Measured electric field vs. time when $1.7\,\mathrm{kV_{rms}}$ 60 Hz voltage is applied on the cylindrical conductor. The expected waveform shows the absolute value of a fitted 60 Hz sine wave.

4.4.1 RF Power Dependency of the Measurement Results

Multiple measurement results show that when the RF power received at the sensor is higher than -8 dBm, it will generate a current in the varactors and results in a shift in the resonance frequency, *i.e.* the mapping graph in Fig.4.11 becomes dependent on the level of the RF power. In the reported measurement results, the RF power of the interrogator was limited such that the received power at the sensor was below the specified level, avoiding added uncertainty due to the impact of the RF power level. Limiting the power level will in turn reduce the maximum achievable interrogation distance. To overcome this limit, the mapping graph in Fig. 4.11 must be power dependent and the received power at the sensor can be estimated by sending an RF impulse to the sensor and deriving the interrogation distance based on the time difference or by manual distance measurement.

4.5 Interrogation Distance

By increasing the interrogation distance, the energy of the received signal at the interrogator will drop, hence reducing the signal to noise ratio (SNR). Therefore, the uncertainty in derivation of the exact peak locations from the ring backs will increase due to the increased noise level. Further, the resolution of the measured results will be lower. The maximum achievable resolution is the minimum detectable change in the electric field strength corresponding to a specific shift in the resonance frequency. In order to derive the maximum achievable resolution, the effect of the noise is quantified for different values of signal to noise ratio (SNR). In this section, the maximum achievable interrogation distance based on the acceptable resolution is derived using the radar equation and is compared to measurement results.

4.5.1 Measurement Uncertainty

The measurement uncertainty is defined as the minimum detectable difference between two consecutive measured resonance frequencies. This error is dependent on the noise received at the receiver (oscilloscope). Further, the resonance frequency is derived from the estimation of the peak locations. Therefore, the estimated peak location and correspondingly the frequency of the decaying sine wave slightly vary from the actual value due to the noise.

The estimated uncertainty in the detected frequency for different signal to noise ratio has been derived in Fig. 4.13. This graph is derived by applying a synthetic, white noise (with Gaussian distribution) to a train of decaying sine waves, similar to the actual recorded ring back with a frequency of 20 MHz (the minimum number of detectable peaks) and a damping time of 5τ. Different values of noise amplitude for different values of SNR are applied over a repetitive decaying sine wave with a known frequency. Then, the signal is analyzed by the peak detection signal processing method. This method is the same analysis applied to the recorded measurement data from the oscilloscope. The signal is filtered and then the period of the peaks determines the frequency of the signals. The standard deviation σ is estimated as the difference between the derived frequencies from the actual frequency. The full width tenth of maximum ($FWTM = 2\sqrt{2ln10}\sigma$ for a Gaussian function) is used as the estimated uncertainty caused by the noise.

One method of decreasing the measurement error is using the averaging method in order to increase the signal to noise ratio. Assuming n is the number of averages, the signal to noise ratio increases by $\sqrt{n}$ while the sampling rate decreases by a factor of n. An averaging of $n = 10$ will result in 10 dB improvement of the signal-to noise ratio SNR in the graph of Fig. 3.7.

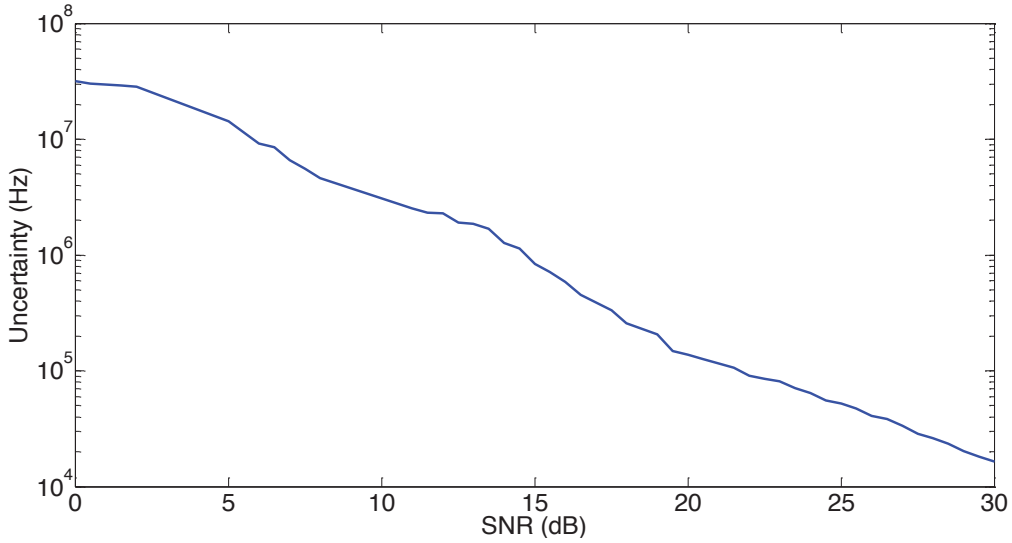

Fig. 4.13: The estimated uncertainty in the derived resonance frequency results versus the signal to noise ratio received at the receiver.

4.5.2 Effect of Resolution on Interrogation Distance

Assuming the acceptable resolution is 50 V/m, a maximum uncertainty of 140 kHz is expected from Fig. 4.13 in the linear range corresponding to a minimum SNR of 20.8 dB. The minimum SNR value dictates the minimum detectable power at the receiver given by [44]

$$P_{r_{min}} = kT \times B \times NF \times SNR_{min} \tag{4.3}$$

where $kT = -174$ dBm is the thermal energy at the room temperature, $B = 40$ MHz is the receiver bandwidth approximated by $B = 0.35/t_{rmin}$ where t_{rmin} is the minimum rise time of the received signal, $NF = 10$ dB is the noise figure of the receiver, and $SNR_{min} = 20.8$ dB is the minimum signal to noise ratio dictated by the expected resolution which correspond to the minimum detectable power of $P_{r_{min}} = -67.18$ dBm at the receiver. The signals at the antenna port and at the oscilloscope port were recorded. A noise figure of $NF = 10$ dB is estimated after analyzing and comparing the results.

4.5.3 Interrogation Distance by Radar Equations

The maximum antenna distance is dependent on the minimum detectable SNR by the receiver and the losses. The radar equation can be used for this interrogation method as the resonator is acting as a scattering object [44]. In this equation, the ratio of the received power to the transmitted power is

$$\frac{P_r}{P_t} = \frac{{G_i}^2 {G_s}^2 \lambda_t^2 \lambda_r^2}{(4\pi R)^4 D\Gamma} \tag{4.4}$$

where P_r and P_t are the received and transmitted powers. The gains of the interrogator and the sensor antennas are G_i and G_s. The losses caused by the resonator such as the return loss of the resonator are shown by $D\Gamma$. Choosing a higher sampling frequency, will decrease the time required for energizing the resonator and introduces losses. λ_t and λ_r are the wavelengths of the transmitted and the received signals. The maximum interrogation distance is then derived from the radar equation as

$$\mathrm{R_{max}} = \sqrt[4]{\frac{\mathrm{P_t}}{\mathrm{P_{r_{min}}}} \frac{\mathrm{G_i^2 G_s^2 \lambda_t^2 \lambda_r^2}}{(4\pi)^4 \mathrm{D\Gamma}}}. \tag{4.5}$$

The maximum achievable distance by the interrogation system is then determined as 6.8 m for $\mathrm{P_t} = 30\,\mathrm{dBm}$ (limited by the ISM band), $\mathrm{G_i} = 15\,\mathrm{dB}$ for a dual polarization broadband horn antenna (model JXTXLB-20180) with 2 GHz to 18 GHz bandwidth chosen for its directivity and high gain, $\mathrm{G_s} = 4\,\mathrm{dB}$ for a LAN antenna (Laird 637113) with a $50\,\Omega$ characteristic impedance, bandwidth of 2.4 GHz to 2.485 GHz and right hand circular polarization chosen for its small size and maximized coverage, $\lambda_\mathrm{t} \simeq \lambda_\mathrm{r} \simeq 0.12\,\mathrm{m}$, and $\mathrm{D\Gamma} = 21.6\,\mathrm{dB}$. The difference in the polarization of the antennas causes a 3 dB extra loss while eliminating the requirement for exact alignment in case of highly directional antennas. The $\mathrm{D\Gamma} = 21.6\,\mathrm{dB}$ loss consists of the 5.6 dB loss calculated in sections 4.2 and 4.3, a maximum of 10 dB loss due to low energy coupling to the resonator, and $2 \times 3\,\mathrm{dB}$

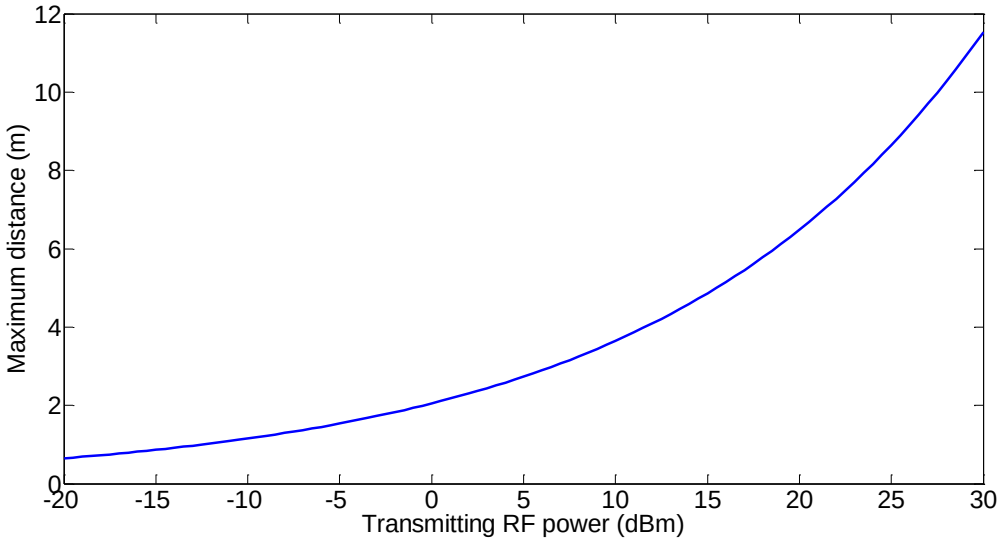

Fig. 4.14: The estimated maximum distance versus the transmitting RF power.

loss caused by polarization difference of the antennas. The loading effect of the antenna is already included in the losses since the quality factor used in sections 4.2 and 4.3 is the loaded quality factor. A maximum of 10 dB loss is also considered which is caused by low coupling derived from S_{11} measurement. Therefore, the total loss associated with the resonator is $D\Gamma = 21.6$ dB due to the losses caused by the time and frequency domain mismatch, antennas different polarization, and energy coupling. The maximum achievable distance versus the transmitting power is shown in figure 4.14.

Considering the RF power dependency of the measurement results discussed in section 4.4.1, the power received at the sensor port must be less than -8 dBm to keep the measured results in the specified range. For an interrogation distance of 6.8 m and -8 dBm of power received at the sensor, ring backs recorded at the receiver will be at -46 dBm of power which is higher than the minimum acceptable power (-67.18 dBm) at the receiver.

Comparing the measured results of the antenna distance with the calculated results shows a significant difference. For example, the calculated FWTM of the recorded signal in

Fig. 4.10 shows an uncertainty of 7.2 kHz corresponding to SNR= 31.6 dB from Fig. 4.13. Therefore, the minimum acceptable power using (4.3) is $P_{rmin} = -65.4$ dBm for a resolution of 7.2 kHz. For a measurement distance of R= 60 cm, the transmitting power is then derived from (4.5) as $P_t = -10$ dBm. The calculated transmitting power in comparison to the actual transmitting power of 7 dBm, measured at the interrogator antenna port, shows a significant difference. The most important reasons for the difference between the calculated and measured transmitting power that results in 7.2 kHz uncertainty are listed below.

- The noises other than the thermal noise are neglected in (4.3).
- Interference from the reflected transmitting signal and other wireless devices working in the ISM band of 2.45 GHz are neglected in the equations.

4.6 Summary

The interrogation system that was proposed, fabricated and tested in this research wirelessly transmits pulses of RF signal using a switch to turn on/off the signal from an RF source. The resonator will re-emit pulses of damped sine wave (ring back) during the time that the transmitting pulse is switched off. The ring backs will be down converted and recorded for processing. The instantaneous resonance frequency of the sensor is derived by determining the peaks' time of each recorded ring back.

The interrogation distance is determined by the minimum acceptable resolution of the measured results. The resolution is the minimum detectable change in the electric field which in turn is dependent on the minimum detectable variation in the resonance frequency. The uncertainty in the determined resonance frequency is dependent on the SNR of the received signal. Considering the thermal noise effect and employing the radar equations, the maximum interrogation distance of 6.8 m is achievable for a resolution of 50 V/m.

Chapter 5

Performance Evaluation

In this chapter, the influence of different parameters on the measurement results are quantified and methods of reducing the uncertainty added by these parameters are discussed. The environmental influences such as temperature and sensor alignment affect the variation of the resonance frequency detected by the interrogator. Therefore, the effect of these parameters (*i.e.* temperature and alignment) must be recorded and employed in mapping of the captured resonance frequency to the corresponding electric field magnitude. Other sources of interference such as environmental noise and reflections, affect the RF signal received at the interrogation system, hence causing uncertainty in the resonance frequency detection. The uncertainty added by the noise and interference is quantified as the resolution of the electric field measurement. The sensor operable range such as the maximum magnitude of the electric field that is measured by the sensor and the detectable range of frequency of the AC electric field that is detectable by the sensor is later quantified in this chapter. The properties of other available electric field sensors are compared to the proposed sensor in this thesis at the end of this chapter.

5.1 Calibration

The calibration method applied to the measurement of the electric field using the proposed sensor in this thesis is based on measuring the resonance frequency variation when a known (medium/high) voltage is applied to the test setup (see Fig. 4.9) with known dimensions. The electric field at the location of the sensor (in the absence of the sensor) is calculated using finite element method simulation. Once the graph that maps the resonance frequency to the corresponding electric field is derived (similar to that shown in Fig. 4.11), it can be employed in the measurement of an unknown electric field surrounding high voltage devices. The mapping graph derived by the above mentioned method is only valid if the influence of environmental parameters, *e.g.* sensor alignment and temperature, are eliminated.

5.1.1 Sensor Alignment

Since the body of the sensor forms an equi-potential surface, the measured electric field is strongest when the electric field lines are perpendicular to the top PCB, as in this situation the voltage induced in the isolated region is the highest. In order to quantify the effect of the sensor rotation, the sensor and the antenna are attached to a circular foam board shown in Fig. 5.1.

The resonance frequency variation corresponding to the known voltage applied to the measurement setup in Fig. 4.9 is derived for different alignment angles of the sensor. The resonance frequency variation is then mapped to the corresponding electric field using Fig. 4.11. The measurement results are shown in Fig. 5.2 as the ratio of the measured electric field to the perpendicular electric field component versus the angle of the sensor. The results verify that the sensor will have the maximum resonance frequency deviation if the measured electric field is perpendicular to the top PCB plate of the sensor. The asymmetry of the graph in 5.2 is the result of the connection of the antenna through the SMA cable on one side of the sensor. The SMA cable will be located on top of the sensor while rotating to

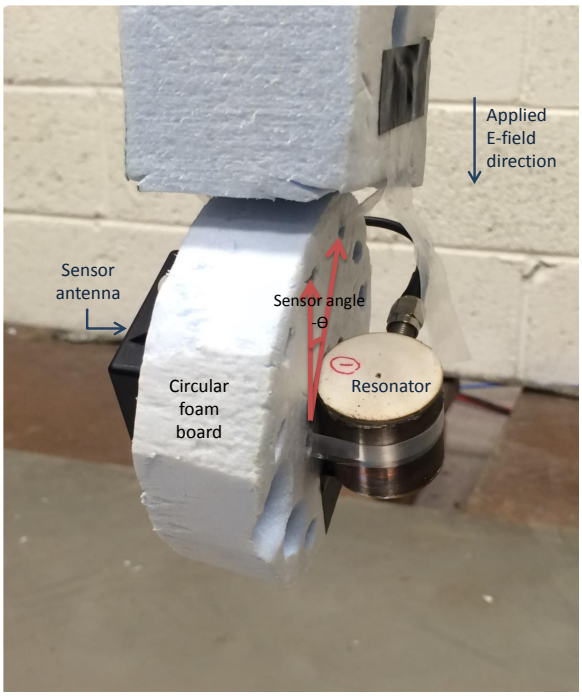

Fig. 5.1: The sensor mounted on a circular foam board. The effect of sensor alignment is measured by rotating the sensor. The reference angle of the sensor towards the electric field is shown by θ.

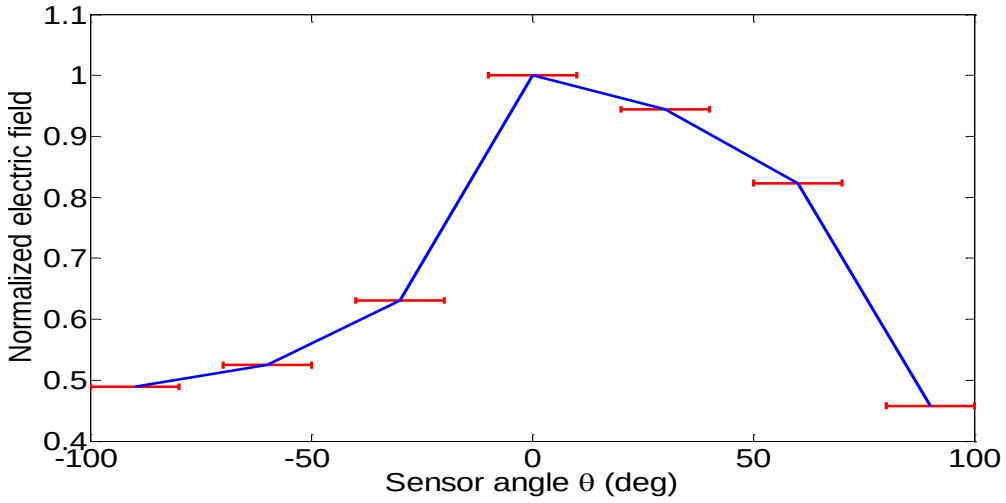

Fig. 5.2: The ratio of electric field amplitude to the amplitude at 90° angle versus the sensor angle. The sensor rotation is assumed to be at 90° angle when the electric field is perpendicular to the top PCB plate. The bars indicate the angle inaccuracy caused by the misalignment of the foam board.

negative θ angle, hence, causing an increase of the induced electric field on the equi-potential outer body of the sensor and correspondingly, a decrease while rotating to positive θ angle.

5.1.2 Temperature Effect

The resonance frequency of the sensor is not highly dependent on temperature changes. With zero-bias on the varactors, the measurement results of varying the temperature from -4 °C to $+56$ °C show an approximate shift of 3 MHz in the resonance frequency. The measurements are conducted by once heating the sensor inside an oven and once cooling it inside a freezer. Then, the temperature and the resonance frequency variation are measured (shown in Fig. 5.3) using a thermocouple and a network analyzer till it settles to the room temperature. The accuracy of the recorded results are within 10 kHz for the recorded resonance frequency.

The resonance frequency of the sensor is influenced by the thermal characteristics of the

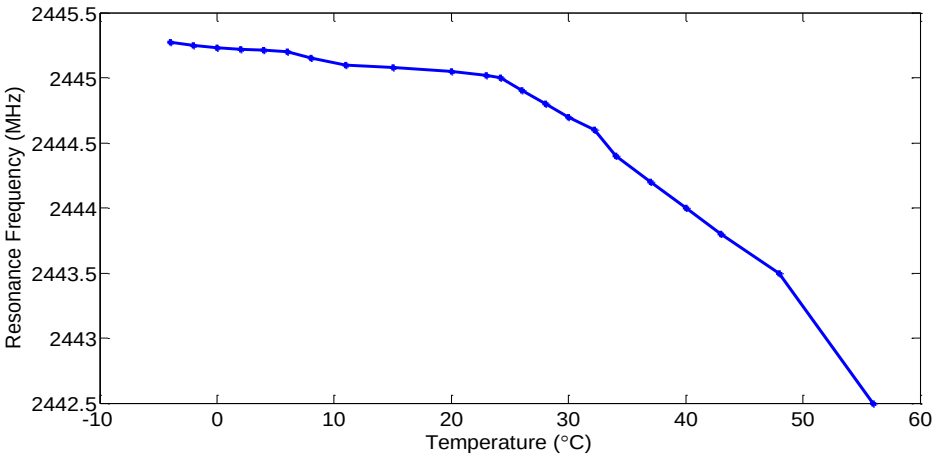

Fig. 5.3: The resonance frequency versus the temperature of the sensor when the varactors are not biased.

PCB dielectric, copper tube and the varactors. The PCB used on top of the sensor (Rogers, RT/duroid 6002) has a thermal coefcient of +12 ppm/°C, Copper has 16.5 ppm/°C and the operable range of the varactor is from −55°C to +125°C. The SMV1231 varactors show an approximate 8% change in capacitance for a temperature variation from −40°C to +80°C. Further measurements are required to derive the overall temperature dependency of the sensor for different bias voltages of the varactors to include the temperature dependency of all the elements inside the sensor.

To compensate for the temperature dependence, a second resonator with similar structure and slightly different resonance frequency ($\geq$ 10 MHz) from the electric field sensor can be mounted close to the sensor as a temperature sensor and interrogated simultaneously to compensate for the temperature-induced variation. The interrogation system has the potential to analyze multiple sensors simultaneously using proper filtering at the receiver. Using temperature dependency information of the sensor, the deviation associated with the temperature changes can be eliminated.

5.2 Resolution

The maximum deviation of the measured electric field from the actual value is considered as the resolution. Full width tenth of maximum (FWTM) deviation of the measured results is calculated as the maximum deviation/resolution of the measured electric field. FWTM is typically used to define the deviation of a signal with added Gaussian noise from the actual signal. Since the typical noises affecting the measurement results (*i.e.* thermal noise) have normal (Gaussian) distribution, the FWTM value is used to define the resolution. The FWTM is calculated by deriving the variance (σ^2) of the deviation of the measurement results from the expected results. Then the FWTM is calculated as FWTM= 4.29σ.

The resolution of the measurement results reported in Fig. 4.12 is presented here as an example. The resolution is calculated as FWTM= 12.5. The value is determined by calculating the variance (σ^2) of the measured results from the known electric field and using FWTM= 4.29σ. Therefore, the resolution is $\Delta E = 12.5\,V/m$ for the reported measurement results.

The calculation of the FWTM of the resonance frequency of the recorded signal in Fig. 4.10 shows an uncertainty of 7.2 kHz as defined in Section 4.5.1. The uncertainty value corresponds to SNR= 31.6 dB using Fig. 4.13. Therefore, the minimum acceptable power using (4.3) is $P_{rmin} = -56.4\,dBm$ for a resolution of 7.2 kHz. For a measurement distance of R= 60 cm, the transmitting power is then derived from (4.5) as $P_t = -1\,dBm$. The calculated transmitting power in comparison to the actual transmitting power of 7 dBm measured at the interrogator antenna port shows a significant difference.

The reason for the difference between the actual and the expected transmitting power for an specific resolution is neglecting some sources of noise and interference in the calculations. Some of the sources adding to the uncertainty of the results and limiting the interrogation efficiency include noises other than the thermal noise, interference from the reflected transmitting signal, the RF power dependency of the resonance frequency, and the

effect of the antenna's impedance variation by the surrounding objects. The estimation of the noise figure (NF) of the receiver is another source of inaccuracy which is required to be quantified accurately. The minimum resonance frequency variation in accordance with the resolution is derived as the minimum derivative of the nonlinear graph in Fig. 4.11 resulting in a sensitivity of $\Delta f_r/\Delta E = 7.2\,(\text{kHz})/12.5\,(\text{V/m})$.

5.2.1 Interference of Scattered Transmitting Signal

The measurement setup inside the laboratory is surrounded by nearby reflectors such as walls and laboratory equipments. As the frequency of the transmitted signal is close (or equal) to the resonance frequency of the sensor, the scattered signal will interfere with the ring backs at the receiver.

The power of the reflected signals can be estimated using the radar equation. Assuming a flat wall is the reflector, located 10 m from the interrogator antenna (shown in Fig. 5.4), the reflected power from the wall and received at the interrogator antenna is given by

$$P_{rs} = P_t(\frac{G_i\lambda_t}{8\pi R})^2 \tag{5.1}$$

where P_{rs} is the power of the scattered signals from the wall that is received at the interrogator, $P_t = 30\,\text{dBm}$ is the transmitting power, $G = 15\,\text{dB}$ is the interrogator antenna gain, $\lambda_t \simeq 0.12\,\text{m}$ is the wavelength of the signal, and $R = 10\,\text{m}$ is the distance of the interrogator antenna from the wall. In this equation the wall is assumed to be a perfect reflector and the loss associated with the reflection is neglected. Hence, $P_{rs} = -6.4\,\text{dBm}$ is received at the interrogator antenna which is 60 dB higher than the the minimum detectable power of $P_{r_{min}} = -67.18\,\text{dBm}$ at the interrogator derived in Section 4.5.2.

The delay between the transmitting signal and the received reflections scattered from

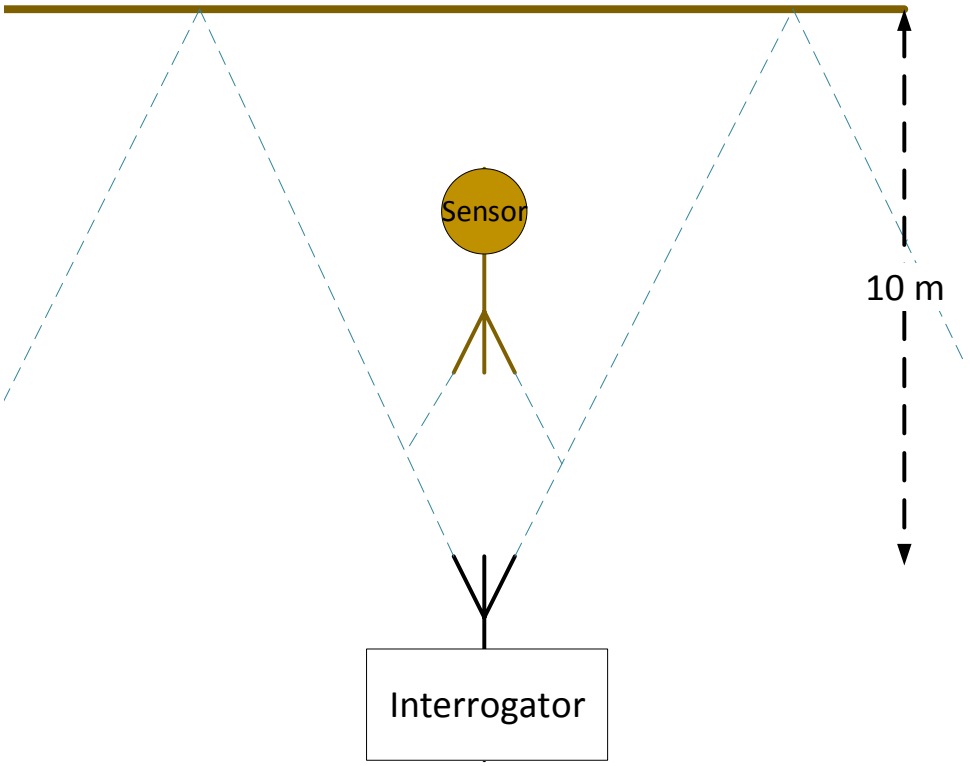

Fig. 5.4: The reflections of the transmitting signal received at the interrogator antenna from a flat wall.

the environment can be estimated using

$$\Delta t_{delay} = \frac{2 \times \Delta d}{\nu} \tag{5.2}$$

in which Δt_{delay} is the delay time required for the transmitted signal to be reflected and captured at the receiver, Δd is the approximate distance between the transmitting antenna and the furthest reflector, and ν is the speed at which the transmitted pulses travel (approximately the speed of light in the air). Assuming the furthest reflector is 10 m away from the interrogator antenna, a 60 ns delay is expected for all the reflections to be received at the interrogator antenna.

In order to reduce the interference caused by the received reflections at the interrogator, a delay must be added to the receiving time periods of the interrogation. Hence, the interrogator will start capturing the received signals (*i.e.* reflections and the ring back) after the strong reflections have faded. The calculated 60 ns delay for the reflections received from a flat wall, is applied to the output of the pulse generator signal in Fig. 4.2 (after a not gate) to control a switch at the receiver. The switch turns on after the latest reflection and impedes the strong reflections to enter the interrogation system and interfere with the ring backs. Further, the ring back time constant $5\tau = 300$ ns in 4.2 considered as the receiving time of the interrogation is 5 times longer than the delay time. Therefore, an acceptable length of the ring back is received by the interrogator in spite of eliminating the first 1/5 of the ring backs.

5.2.2 Flicker Noise Caused by SMD Thick Film Resistor

Thick film resistors are known for their high flicker (1/f) noise. The flicker noise power decreases with the signal frequency increase. In order to study this effect on the overall noise of the system, AC electric potential with different frequencies was directly applied over the varactors and the variation in the resonance frequency was interrogated. The

direct voltage is applied through a 100 kΩ resistor electrically connected to isolated region of the sensor. The change in the frequency of the bias voltage of the varactors did not indicate added noise to the measured results. A range of 10 Hz to 5 kHz bias voltage shows the same noise level received at the interrogator. Therefore, flicker noise is not a major source to add noise to the measurement results.

5.2.3 Antenna Impedance Variation

Presence of objects near the antenna of the sensor will change the impedance of the antenna which in turn changes the resonance frequency of the resonator. In order to analyze this effect, a series of measurements have been conducted on a two port resonator with a similar configuration as the sensor. One port of the resonator is connected to a network analyzer and the other port is connected to the sensor antenna (Laird 637113) as shown in Fi. 5.5. The SMA pin on the antenna side is fixed to measure $S_{11} = -8$ dBm and the SMA pin on the network analyzer side is fixed to measure $S_{11} = -30$ dBm for maximum coupling. An aluminum plate ($30 \times 30\,\text{cm}^2$) is placed at a distance of 2 cm from the antenna at each side and in the front of the antenna. The S_{11} parameter measurement results show a maximum resonance frequency variation of 6 kHz which is less than the derived resolution of 7.2 kHz. The experiment was repeated by moving one's hand in front of the antenna resulting in similar resonance frequency deviation. The maximum deviations recorded are shown in Table 5.1 The main reason for low sensitivity of the sensor to the antenna impedance is the small coupling capacitor of the SMA pin that is in the order of 0.2 pF.

5.3 Maximum Measurable Electric Field

The maximum measurable electric field using the sensor is limited by the varactors' characteristic linear range and is dependent on the resistor R shown in Fig. 4.8. For a given value of R (475 MΩ in the measured results), measurable electric field up to 7 kV/m is determined

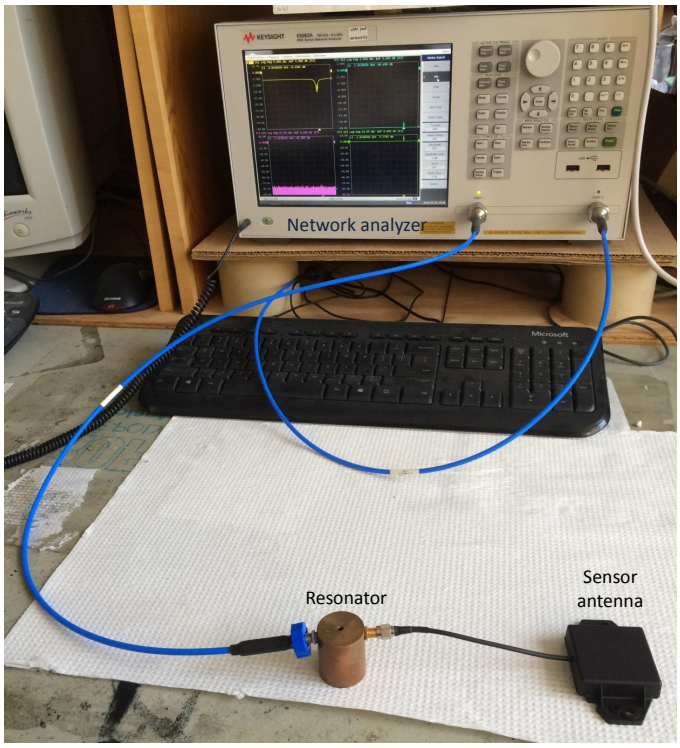

Fig. 5.5: Measuring the effect of other objects in close proximity to the antenna of the sensor. A resonator with similar dimensions to the sensor and two SMA ports on the sides is connected to the network analyzer on one SMA port and the antenna on the other. The changes of the S-parameters are recorded on the network analyzer for different objects moving close to the antenna.

Table 5.1: The resonance frequency shift caused by the changes in the antenna impedance corresponding to close distance objects.

Objects	Maximum shift in resonance frequency (kHz)
One's Hand	3
Aluminium Plate	6

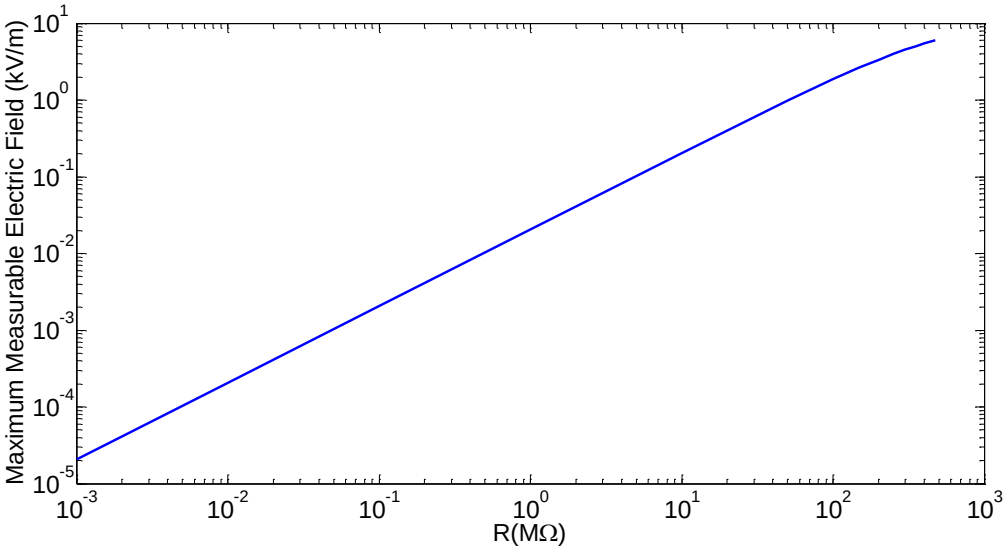

Fig. 5.6: The maximum measurable electric field by changing R, the resistor in parallel with the varactors.

by increasing the applied voltage until the operating point of the varactor is outside the linear region of Fig. 4.11. The measurable range of the sensor calculated for different values of R using the equivalent circuit of Fig. 3.4 is shown in Fig. 5.6 . Increasing this range by increasing the resistor R results in lower sensitivity and resolution. These two parameters decrease linearly with an increase in the measurable electric field range.

5.4 Frequency Bandwidth

There are two mechanisms that independently determine the bandwidth or the frequency range of the AC electric field signals that can be recorded using the proposed sensor. The limitations are imposed by

- Speed of the interrogation system
- Sensor structure.

We have demonstrated that the interrogation system is capable of delivering a readout in about $1/f_{si} = 1/50\,\text{kHz} = 20\,\mu s$ Therefore, the interrogation system (using an averaging of n = 50) is able to measure transient signals (such as switching impulses) with risetimes in the order of ms. The upper cutoff frequency of the measurable electric field using the passive wireless sensor imposed by the interrogation system is less than 250 kHz (without averaging). The cutoff frequency of 250kHz is determined assuming a 2.5MHz sampling rate of interrogation and requiring a minimum of 10 samples for detecting a sine wave electric field.

The sensor's upper cutoff frequency is limited by the operating frequency of the varactors which is less than 1 MHz. Therefore, the upper cutoff frequency is limited by the interrogation sampling rate, (*i.e.* 250 kHz< 1 MHz) which is less than 1 MHz upper cutoff frequency dictated by the sensor.

The lower cutoff frequency is determined by the minimum current of the varactors in reverse bias. Therefore, using the equation

$$I = C_{var}\frac{dV}{dt} = C_{var}\frac{d}{dt}(A_V Sin(\omega t)) = C_{var}A_V \times \omega Cos(\omega t) \tag{5.3}$$

where I is the required reverse bias current, ω is the angular frequency, C_{var} is the capacitance of the varactor, and A_V is the induced voltage over the varactors. Therefore, the minimum operable frequency is determined by the minimum reverse bias current of the varactors ($I_s = 0.01$ pA) using

$$C_{var}A_V\omega Cos(\omega t) \geq 0.01pA \tag{5.4}$$

.

In 5.4, for maximum varactor capacitance $C_{var} = 2.35$pF, and Cosωt = 1, the minimum acceptable frequency (Ω) with a voltage magnitude in the range of a few volts will be in

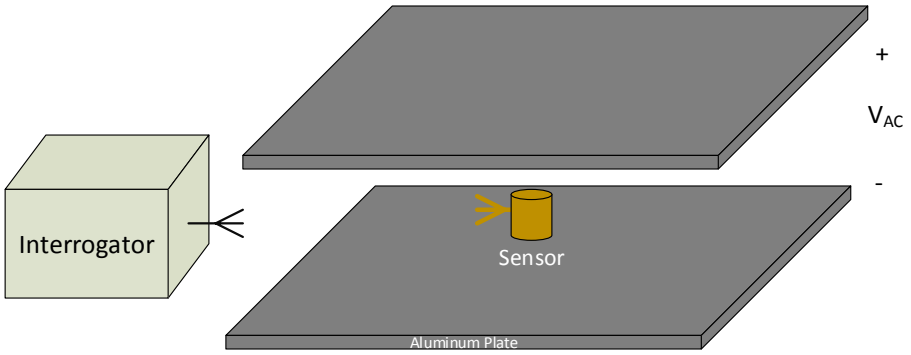

Fig. 5.7: Setup for measuring AC electric field with different frequencies. The sensor is placed between the parallel aluminum plates inducing the electric field.

the range of mHz.

In order to verify the operable frequency bandwidth of the sensor with measurement results, a setup as shown in Fig. 5.7 is used. The sensor is placed between two parallel plates of aluminum with a separation of 10 cm. An AC voltage in the frequency range of 30 Hz to 1 kHz and 100 V is applied to the plates using an amplifier (AE Techron 7224). The sensor is directly connected to the interrogator without the use of antennas to reduce the interference of the reflected signals from the aluminum plates. The results in Fig. 5.8 show the resonance frequency variations. The result of the 30 Hz AC electric field measurement is significantly affected by higher frequency noise and interference. In Fig. 5.8, the inaccuracy of the measured results near zero increases where the inducing voltage has frequencies higher than 1 kHz. By increasing the frequency, the changes near zero electric field will be sharper hence the inaccuracy of the measured results near zero (due to the discharging time of the varactors discussed in 4.4) increases.

The maximum shift in the resonance frequency of the sensor varies due to the frequency of the inducing electric field as shown in Fig. 5.8. Hence, the sensor acts as a bandpass filter for the electric field. The attenuation caused by the filtering characteristic of the sensor

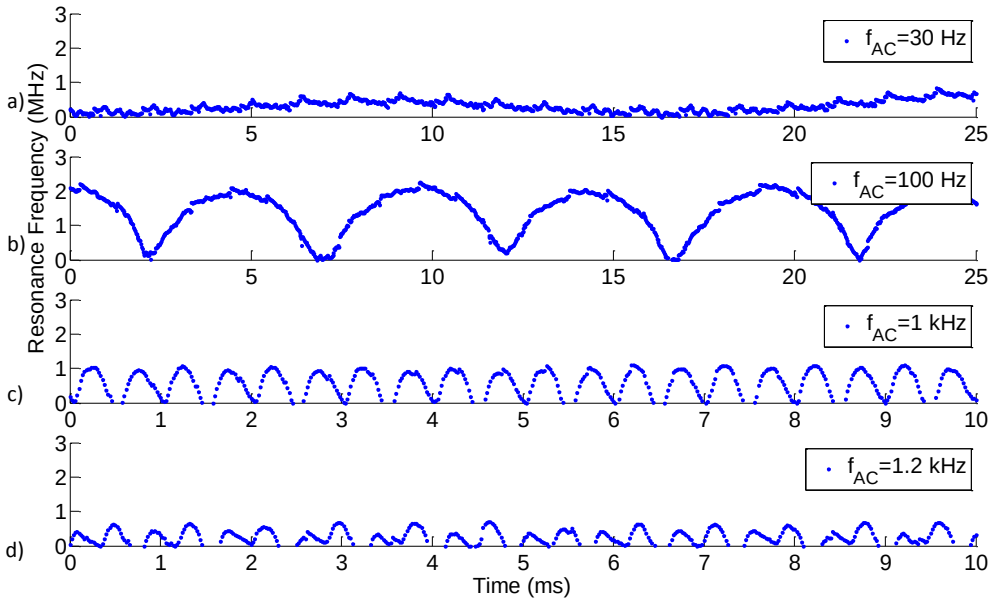

Fig. 5.8: The electric field measurement results for electric field with constant amplitude 1 kV/m and frequencies of a) 30 Hz, b) 100 Hz, c) 1 kHz, and d) 1.2 kHz.

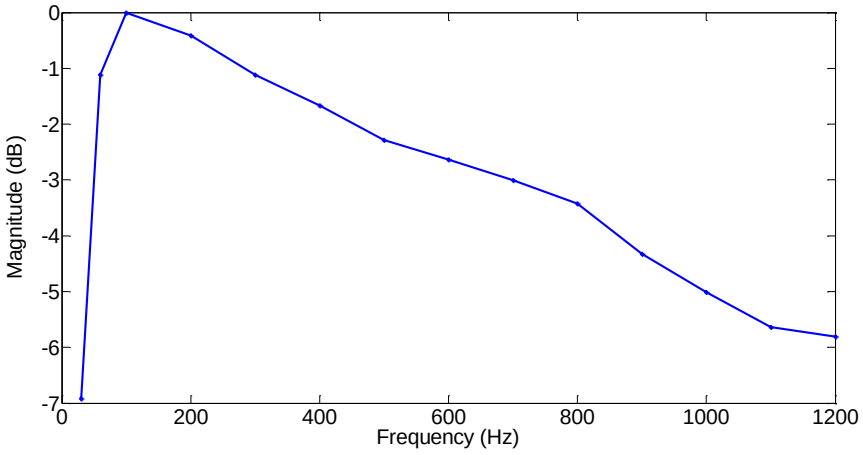

Fig. 5.9: The bandpass filtering characteristic of the sensor with $R = 475\,\mathrm{M}\Omega$.

is shown in Fig. 5.9. This graph is derived for the sensor with an internal resistance of $R = 475\,\mathrm{M}\Omega$.

5.5 Comparison with Other E-field Sensors

The properties of the proposed passive wireless electric field sensor is compared with three sensors applicable in high voltage measurements in Table 5.2. The MEMS sensor [29] is comparable to the proposed sensor and has the advantage of significant small size. However, the reported sensor requires vacuum packaging increasing the overall size of the sensor and the interrogation is done through direct electrical connection. The MEMS sensors are still at the research stage. The optical sensor is a prototype developed by Kapteos [26,27] with very high resolution and the required electrical isolation from high voltage systems. Although this sensor/probe is claimed to be electrically passive, it requires direct connection to a laser transceiver. The electric field mill reported in [60] is an active sensor developed by Nasa's Jet Propulsion Laboratory for DC electric field measurement. The size of the sensor has been significantly reduced in comparison to the conventional field mills.

Table 5.2: Comparison of the properties of three electric field sensors applicable in high voltage measurements. The resolution of the proposed sensor is reported for the 60 cm interrogation distance and 7 $d\mathrm{B}m$ transmitting power. The interrogation distance is a variable of the required resolution and the transmitting power.

Properties	MEMS Sensor [29]	Optical Sensor [26, 27]	Field Mill [60]	Proposed Sensor with R= 475 MΩ
Measurable E-field range	42 V/m – 6 kV/m	≤ 100 kV/m	100 V/m – 500 kV/m	200 V/m – 7 kV/m
Resolution	42 V/m	0.7 V/ m/$\sqrt{\text{Hz}}$	2% of Measured E-field	≃ 12.5 V/m
Sensor/probe Dimension	4 × 4 × 4 mm	10×10×22mm	20 × 20 × 50 mm	30 × 30 × 30 mm
Operating Bandwidth	Not Reported	1 kHz – 10 GHz	DC	10 Hz – 1 kHz
Passive vs. Active	Active	Active	Active	Passive
Remote Interrogation Distance	Direct Connection	Direct Connection	Direct Connection	potentially ≥ 5 m

5.6 Summary

In this chapter, the performance operation of the sensor is discussed with considering the effects of the temperature and the sensor alignment. The sensor approximately shows 3MHz shift in resonance frequency for the temperature variation from $-4\,^{\circ}\mathrm{C}$ to $+56\,^{\circ}\mathrm{C}$. The measurements conducted for specifying the effect of the sensor alignment shows that the maximum shift in the resonance frequency happens when the electric field is perpendicular to the PCB plate of the sensor. Further, the resolution of the interrogation method is calculated as 12.5 V/m. The inaccuracies caused by the parameters affecting the resolution such as flicker noise, interference, and antenna impedance are quantified and shown to be lower than the specified resolution. The measurement results reported in this chapter show a maximum measurable electric field of 7 kV/m and the measurable frequency bandwidth of 10 Hz to 1 kHz. A the end of this chapter, the properties of the sensor are compared with three available electric field sensors applicable to high voltage measurements. The sensor shows acceptable characteristics while providing a passive and wireless measurement method.

Chapter 6

Applications of the E-Field Sensor in the Vicinity of Medium or High Voltage Apparatus

Unlike other electric field sensors, the proposed sensor in this thesis is passive, which creates a unique competitive advantage in most applications, such as safe high voltage measurement from a distance. This chapter demonstrate some applications such as remote measurement of medium/high voltages and detection of possible defects in composite insulations. The efficiency of the proposed sensor in these two applications is verified with experimental examples presented in this chapter.

In section 6.1, the proposed sensor is employed to derive the voltage of an energized single phase conductor. The voltage is obtained from the measured electric field surrounding the high voltage conductor using the proposed sensor. The mapping of the measured electric field to the voltage of the high voltage conductor uses the known dimensions of the setup such as the distance of the conductor from the ground. Further, a method is proposed to enable calculation of the voltage profile using the proposed sensor even if the distance

between the conductor and ground is unknown.

Another application of the proposed sensor in detection of defects surrounding an insulator is demonstrated in section 6.2. The sensor is employed to measure the deviation of the electric field profile in the presence of a defect in comparison to a healthy insulator. The experimental results show that these methods are very promising and encourage further research in future.

6.1 Measurement of Medium or High Voltage

In power networks, transmission lines often span a long distance, ranging from a few kilometers to hundreds of kilometers. The voltage magnitude across a long transmission line varies from location to location in the line and time to time, *e.g.* depending on heavy or light loading conditions. The distributed voltage profile across a transmission line greatly affects the power transmission capacity of the line as well as the power quality delivered to the customers. As a result, the distributed voltage measurement provides essential information for condition monitoring of power grids which enables utilities to optimally deliver the power to the consumers with minimum transmission losses and costs [3].

The conventional high voltage measurement methods employ voltage dividers and transformers to measure the stepped down voltage. A number of contactless voltage measurement techniques have been proposed to mitigate the deficiencies caused by direct electrical contact of the conventional voltage measurement methods to the power system devices (*i.e.* loading and transformer saturation). Some of the techniques operate by calculating the voltage from the measurement of electric field spatial profile in the vicinity of an energized conductor. The electric field measuring devices employed in voltage measurement are typically optical sensors [61] or contactless capacitive detectors [11, 12, 62] discussed in Sections 2.1.3 and 2.1.4.

The proposed application of the contactless passive wireless sensor for the measurement

of medium or high voltage is studied in this section. The resonance frequency of the sensor varies by the external 50/60 Hz electric field which is directly related to the voltage variation on the high voltage apparatus. The main objective of this section is to develop further techniques to appropriately calibrate the proposed sensor to derive accurate voltage values from the measured electric field. The following steps are discussed in this section in order to verify the application of the sensor for contactless voltage measurement.

- The sensor is placed over the ground and the mapping graph of the electric field versus the resonance frequency of the sensor is derived using an energized cylindrical conductor above the ground.
- In order to verify that the derived mapping graph is not dependent on the conductor distance to the ground, the derived mapping graph is employed in the measurement of the electric field by changing the distance of the conductor to the ground.
- The voltage of the energized conductor is calculated using the measured electric field value and the equation of the electric field surrounding an energized conductor over ground. The equation is employed for the known dimension of the measurement setup, *i.e.* diameter and distance of the conductor over the ground.
- Using multiple sensors at different locations is proposed as a method for calculating the voltage of the conductor without knowing the distance of the conductor to the ground and later verified by measurement.

The sensor is placed at a number of locations between an energized conductor and the ground and at each location, the electric field is measured by interrogating the sensor. From analyzing the recorded measured electric fields at different locations, a general method is proposed to obtain the voltage magnitude of the conductor from the measured electric fields without knowing the distance between the conductor and the ground. In this experiment,

the sensor was repositioned every time for multiple electric field measurements due to the limitations of the available interrogation system. However, in real-life applications, a better practice would be to install multiple sensors in different distances from the conductor and interrogating every sensor separately.

6.1.1 Remote Voltage Measurement for a Known Distance

An energized cylindrical conductor over ground is used to demonstrate the voltage measurement using the proposed sensor assuming that the distance between the conductor and the ground is known. The electric field sensor is placed on the ground below the conductor (see Fig. 6.1). The induced electric field below the conductor and over the ground is calculated with the equation

$$\mathrm{E(y)} = \frac{\mathrm{V_0}}{\ln(\frac{\mathrm{2d\text{-}a}}{a})} \times (\frac{1}{d+y} + \frac{1}{d-y}) \tag{6.1}$$

The electric field E(y) induced by the energized cylindrical conductor with a voltage magnitude of $\mathrm{V_0}$, and a conductor radius a at any point right under the conductor (*i.e* coordinates $x = 0$ and $z = 0$) and the ground at a distance of y from the ground can be calculated using (6.1), where d is the distance between the conductor and the ground in (6.1).

The experiment of deriving the electric field and consequently the voltage of the single phase line over ground is conducted in two steps described in following subsections.

Derivation of the Electric Field Versus the Shift in Resonance Frequency

The resonance frequency of the sensor depends on the electric field at the location of the sensor as was derived and shown in Fig. 4.11 in the previous chapter. This relationship between the electric field and the resonance frequency is however nonlinear and highly depends on the sensor parameters. For example, two sensors with the same structure but even slightly different parameters, such as unavoidable differences between the varactors

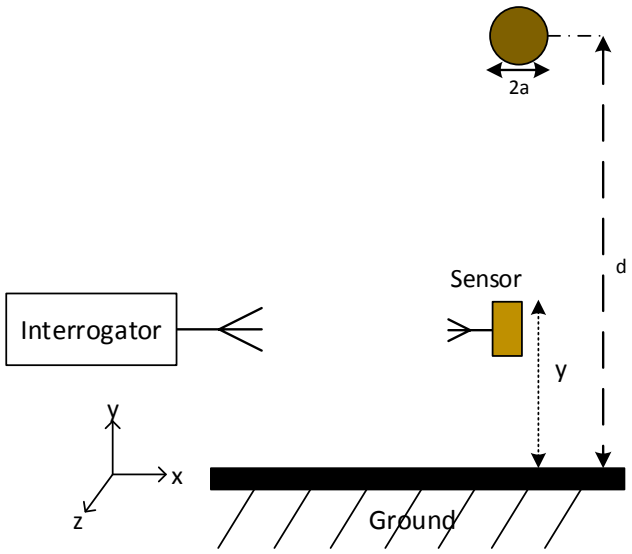

Fig. 6.1: Measurement setup consisting of a circular energized conductor over a large ground plane. The sensor is placed on the ground and electrically grounded.

manufactured by a company or slight errors in sensor fabrication, could yield two different E- mapping graphs. As a result, for every new sensor, this graph must be derived. The graph derived for this section is for the sensor located on the ground and electrically connected to the ground. The electrical connection of the body of the sensor to the ground changes the induced voltage over the varactors for a specific electric field in comparison to the sensor floating (without electrical connection) in the vicinity of the same electric field. Hence, the resonance frequency mapping graph differs. The difference is resulted by the forced ground potential over the body of the sensor in one case in comparison to the floating case where the body of the sensor will reach equi-potential depending on the average voltage induced over the length of the sensor.

In an experiment, the conductor is placed and fixed at 73 cm above the ground. The voltage of the conductor is changed from 0 to 12 kV in 12 steps. At each voltage level, the shift in the sensors resonance frequency is measured. Knowing the voltage magnitude of the conductor V_0, the distance between the conductor and the ground (d = 73 cm), the radius of the conductor (a = 1.19 cm), and the measurement point height (y = 3 cm), the corresponding electric field magnitude is numerically calculated from (6.1). Please note that in this section, the sensor is always placed at the ground underneath the conductor and hence the measurement points height is always the height of the sensor, which is y = 3 cm. Also, all voltage and electric field measurements and calculations are obtained based on the peak values of the measured waveforms. This procedure is completed for all voltage levels and the electric field versus Δf mapping graph shown in Fig. 6.2 is obtained. This mapping graph is independent of the external parameters, such as the distance between the conductor and the ground d as well as the conductor radius a, *etc.* Therefore, this derived mapping graph can be used in all measurements using the same sensor where the sensor is electrically connected to the ground. However, the voltage versus the resonance frequency graph varies if any of the parameters d, a, or y changes.

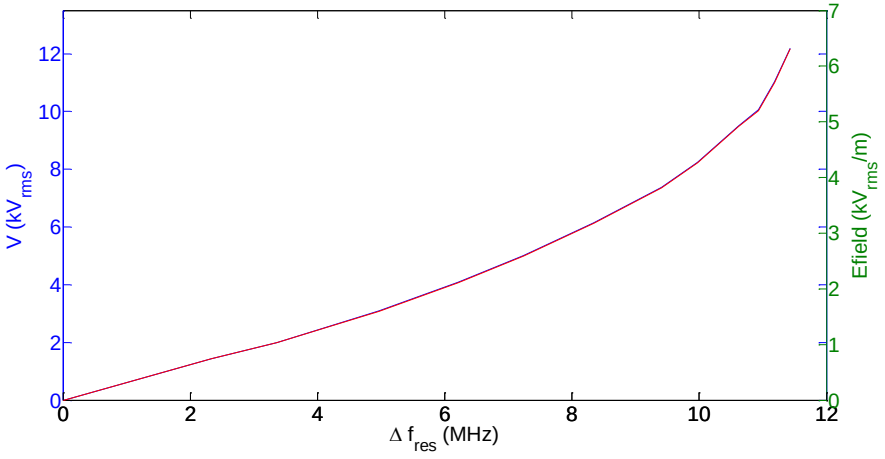

Fig. 6.2: The voltage of the energized conductor versus the resulted resonance frequency derived by measurement and the corresponding electric field.

Voltage Estimation Validation

In this step, the derived mapping graph (electric field versus Δf) in Fig. 6.2 is used to determine the voltage magnitude of the conductor using (6.1), knowing the values of different dimensions, *i.e.* d, a, and y. As mentioned above, the mapping graph is independent of the external dimensions and can be used for different setups. For instance, in the following, the conductor is placed once at d = 58 cm and once at d = 98 cm and every time a variety of known voltage magnitudes are applied to the conductor. For every voltage magnitude applied to the conductor, the resonance frequency of the sensor is measured and recorded. The corresponding electric field is found from the mapping graph in Fig. 6.2. Finally, the estimated voltage magnitude is numerically calculated from (6.1). The voltage estimation using the proposed method is valid if the estimated voltage magnitude from (6.1) is similar to the expected voltage magnitude which is known as the voltage magnitude applied to the conductor. This is repeated for all voltage steps and for both different conductor distances from the ground.

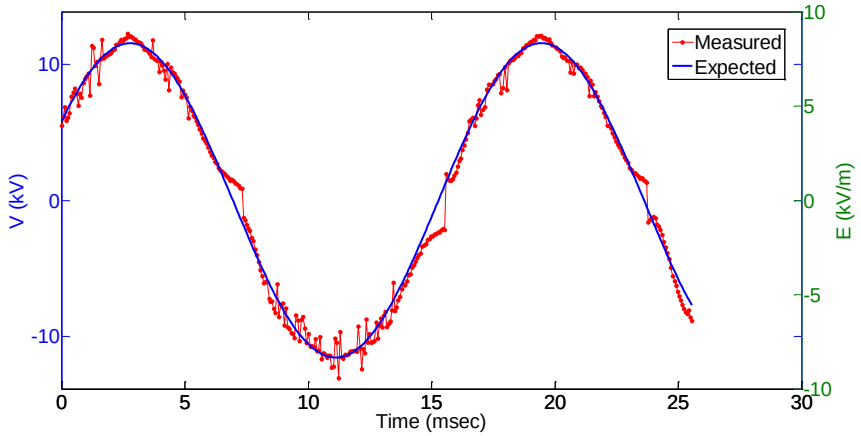

Fig. 6.3: The electric field variation by time derived and the inducing voltage for d = 58cm and a 60 Hz AC voltage with V = 8.18 kV_{rms}. The inducing voltage on the conductor is calculated using (6.1).

The estimated voltages agreed with the expected values in all set points. As an example, in Fig. 6.3, the measured result of the energized conductor over ground for d = 58 cm and V = 8.18 kV_{rms} is shown. The estimated voltage waveform from measuring the resonance frequencies of the sensor through a 60 Hz cycle is compared to the expected voltage values of the sine wave.

The deviation of the estimated results from measurement in comparison to the expected values are shown in Table 6.1. The values in Table 6.1 are derived by measuring the electric field of multiple known voltages for two conductor heights, d = 58 cm and d = 98 cm, and comparing the derived voltages from measurement with the known voltage values. The values reported in Table 6.1 are derived as the ratio of the maximum deviation of the measured peak to the expected peak voltage. The deviation is a result of the approximations in 6.1. This equation is derived using approximations such as infinite conductor and an infinite ground.

Table 6.1: Deviation of the measured results from the expected voltage

	For d = 58 cm	For d = 98 cm
Mean deviation (%)	1.7	1.3
Max deviation (%)	2.4	3.8

6.1.2 Remote Voltage Measurement for an Unknown Distance

The reported measurement results in Section 6.1 verified the feasibility of applying the same electric field versus resonance frequency mapping graph for different measurement scenarios (*e.g.* different dimensions of d, a, or y) using (6.1) to obtain the voltage of an energized conductor without electrical contact. The results in the previous section were derived assuming that the dimensions of the measurement setup and its distance over ground are known. Since in high voltage measurements, it is difficult, hazardous, and sometimes infeasible to know the exact values of d and y to calculate the voltage, an adaptive self-calibrating method is required.

The measurement setup for the proposed calibration technique is presented in Fig. 6.4. A number of sensors (two in this example) below the energized conductor are measuring the electric field at different distances from the conductor. Assuming the sensors are mounted at specific locations on an insulator, the distances (Δy_1 and Δy_2) are known. Therefore, the unknown values of d and V_0 can be derived by curve fitting using (6.1). In practice, the value of the conductor radius (a in 6.1) is typically known based on the conductor specifications but the distance d varies due to change in the overhead conductor sagging caused by ice buildup or heating.

In order to verify the proposed method for the measurement of a single phase voltage, the results of measuring the electric field profile using one sensor at different heights below a single phase conductor is recorded. This method is employed as an alternative to the

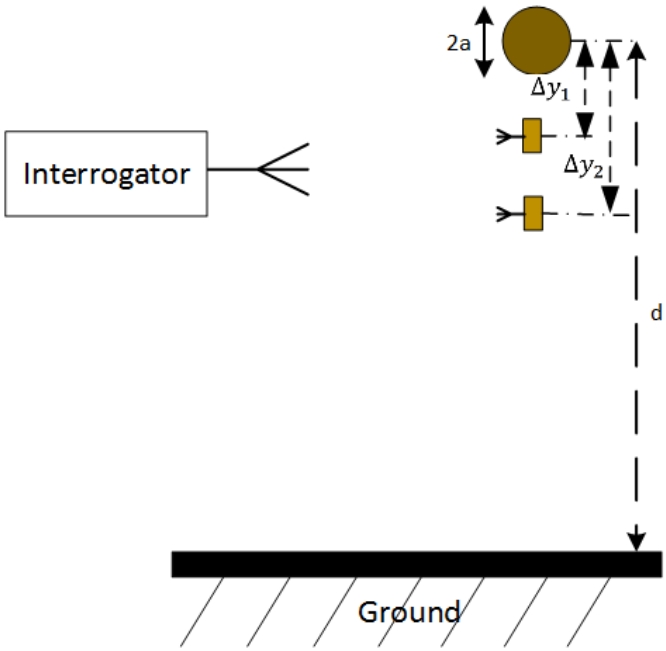

Fig. 6.4: Measurement setup for the adaptive self-calibrating method for contactless voltage measurement.

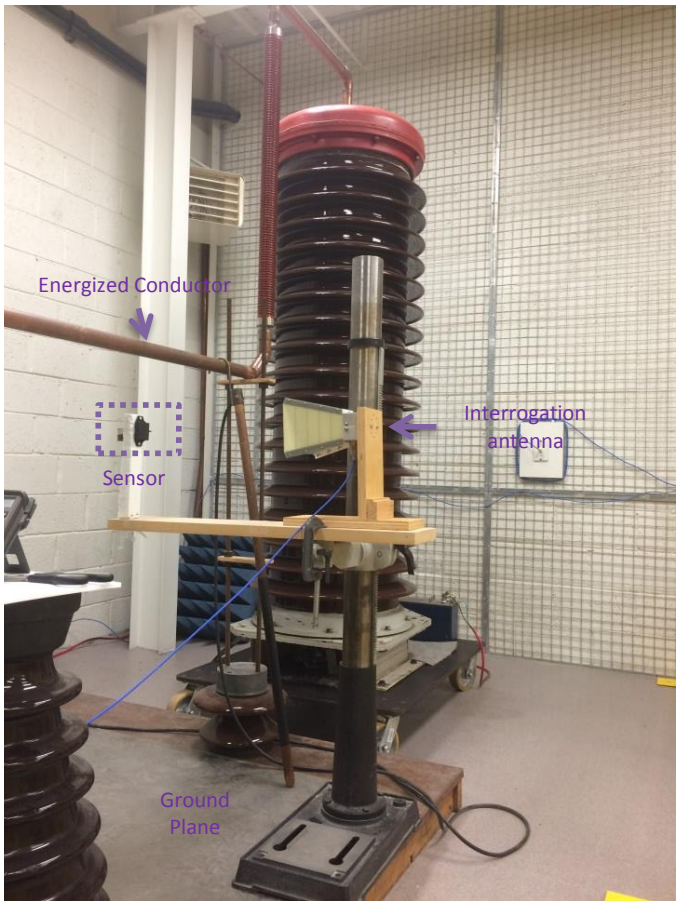

Fig. 6.5: Voltage measurement setup using the measured electric field by a sensor at different heights.

simultaneous measurement of multiple sensors since the available interrogation system is not adapted to measuring multiple sensors. The sensor and the interrogation antenna are clamped to an adjustable nonconductive platform as shown in Fig. 6.5. The electric field surrounding the single phase conductor is then measured at different heights for a known voltage.

Typically, the RMS value of the 60 Hz signal is of interest in the measurement of voltage in power applications (*i.e.* transmission and distribution lines). Hence, the setting of the oscilloscope has been altered in comparison to previously reported measurements to

capture a larger time frame (107.4 ms) with less repetition of samples (2.5 GSamples/s) in order to keep the storage memory constant. The maximum available memory is a limitation imposed by the oscilloscope settings. Reducing the sampling rate increases the uncertainty in detecting the peaks of the ringbacks reported in Fig. 4.13. The reported measurements in Chapter 4 are recorded with 10 GSamples/s. The increase in the uncertainty (reported in Fig. 4.13) as a result of the reduced sampling rate is then estimated to be 50 kHz.

A sample of the recorded results is shown in Fig. 6.6. The sensor is measuring the voltage of a single phase conductor energized by a 60 Hz AC signal with a peak voltage of 4620 V. The conductor and the sensor are respectively located at 120 cm and 100 cm above the ground. The measured resonance frequency is mapped using the graph (electric field versus resonance frequency) in Fig. 4.11. In Fig. 6.6, the RMS value is derived from a limited time frame of the signal including 6 periods of the measured absolute value of a 60 Hz AC signal. Limiting the time frame to include a number of complete periods of the sine wave decreases the error in the calculation of the RMS value. The fluctuations around the peaks is a result of the noise and interference which has more influence on the bias voltage of the varactors around the settling time. The varactors are sensitive to the derivative of the electric field which is minimum around the peaks. Hence, the increase in the noise level at the peaks in Fig. 6.6 is expected.

The measured RMS values of the electric field for various height levels above ground are reported in Table 6.2. The reported electric field values are obtained from mapping the measured shift in resonance frequencies to the electric field using the mapping graph in Fig. 4.11. The expected values of the electric field at each location is also reported which is calculated using (6.1).

In order to calculate the voltage and the distance of the conductor above ground, the measurement results are used in curve fitting to find the electric field profile. Equation (6.1) is altered to include the known constant Δy (the distance of the sensor from the energized

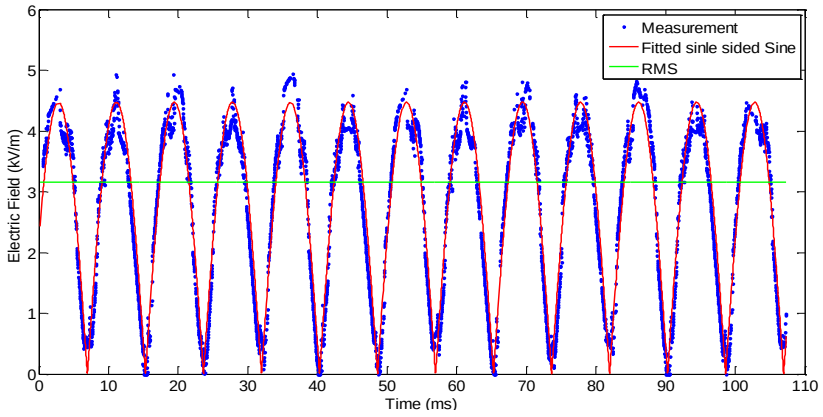

Fig. 6.6: Electric field measured around a single phase conductor over ground. The time frame of the captured signal is increased to 107.4 ms with the decrease to 2.5 GSamples/s in the sampling rate.

Table 6.2: Measured electric field at different height levels below a single phase conductor placed 120 cm above ground for two known voltages applied to the conductor.

Conductor Voltage (kV_{rms})	Distance from the conductor (Δy) (cm)	Measured E-field (kV_{rms}/m)
7.75	34	5.54
	31	6.08
	28	6.73
	25	7.68
	22	8.05
	19	8.44
5.75	34	3.84
	31	4.36
	28	4.57
	25	5.38
	22	5.96
	19	6.60

conductor) in (6.2) and be used for curve fitting.

$$\mathrm{E} = \frac{\mathrm{V}_0}{\ln(\frac{\mathrm{2d\text{-}a}}{a})} \times (\frac{1}{2d - \Delta\mathrm{y}} + \frac{1}{\Delta\mathrm{y}}) \tag{6.2}$$

In this equation, the known values are assumed to be the value of the measured electric field (E), the distance of the sensor to the conductor (Δy) and the conductor radius (a).

The curves fitted to the measurement results are shown in Fig. 6.7. The fitted curves are calculated by finding the minimum least square deviation of the measured electric field values from the fitted curves using the predefined nonlinear solver algorithm in Matlab. The solver finds the values of d and V_0 in (6.1) that minimizes the deviation of the fitted curve from the measured electric field. Precise values of the voltage can be obtained by further limiting the distance d to values close to the actual distance. If exact value of d is unknown, still a good estimation of the voltage can be obtained by using an approximation of d.

In order to find the best fitted curve for the electric field profile, the electric field values at two or more height levels are required. In Table 6.3, the measured electric field values at two and three height levels are chosen to find the voltage. The approximate value of d is assumed to be known with a deviation of $(1 \pm 0.05)\,d$ in the calculations. The maximum and minimum deviation of the calculated d and V_0 values from the expected results using the measured electric fields at two or more height levels are reported in Table 6.3. The deviation from the expected results is calculated as the least square error (LSE) and the results with the minimum and maximum LSE are reported as the best and worst fit. The reported results in the table shows that with more number of measured electric field values (number of sensors), the accuracy of the distance-independent method increases. The deviation of the calculated voltage is shown in Fig. 6.8.

The reported results in Table 6.3 verify that by knowing the estimated geometry of a medium/high voltage setup, the voltage can be calculated remotely using the electric field

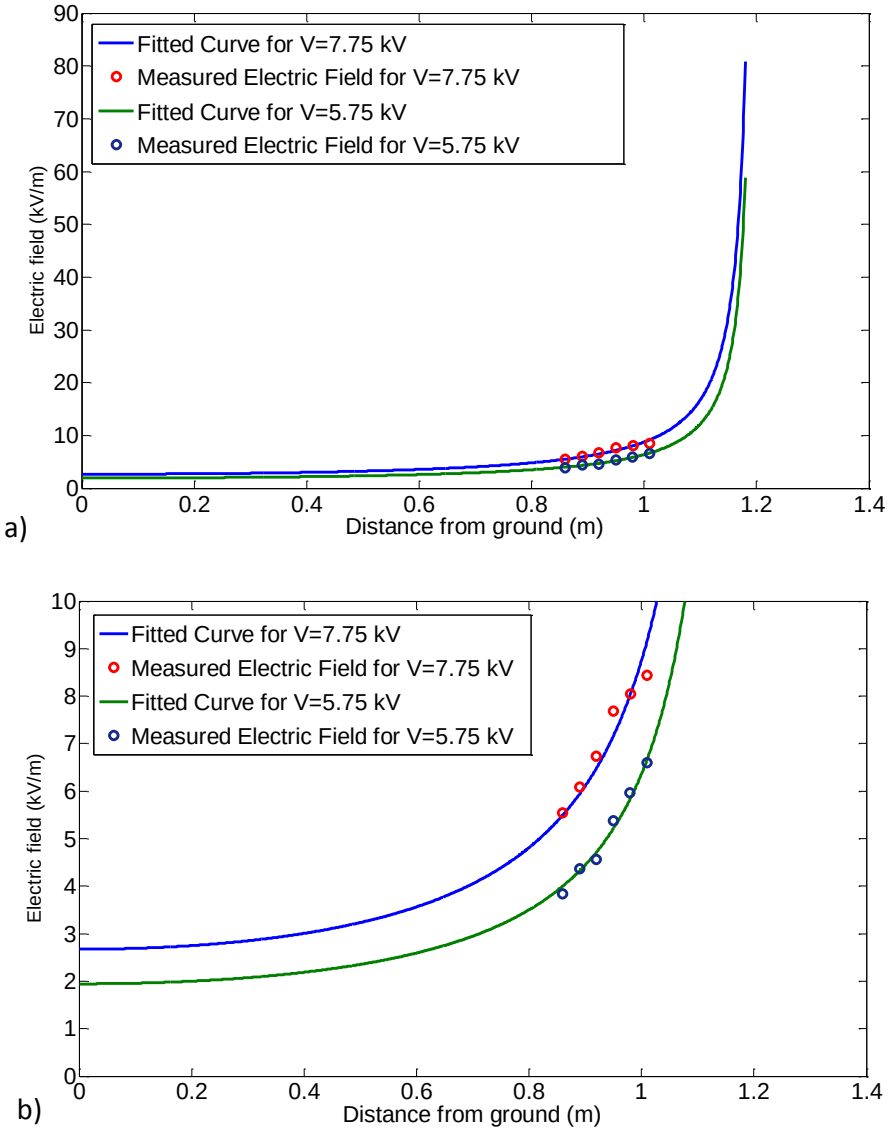

Fig. 6.7: The curve of electric field profile derived by curve fitting to the measured electric field at different heights above ground, a) the electric field profile from ground to the energized conductor, b) the zoomed-in graph of part a on the points of measurement.

Table 6.3: The voltage and the conductor distance from ground calculated by curve fitting to equation 6.2. The Minimum and maximum deviation from the expected V_0 and *d* are reported for the cases of using the measured electric field at two,three and four heights.

	Best results		worst results	
Number of measured e-field points (Number of sensors)	V_0 (kV_{rms})	d (cm)	V_0 (kV_{rms})	d (cm)
2	5.67	120	5.53	126
3	5.68	120	5.61	126
4	5.62	120	5.59	126

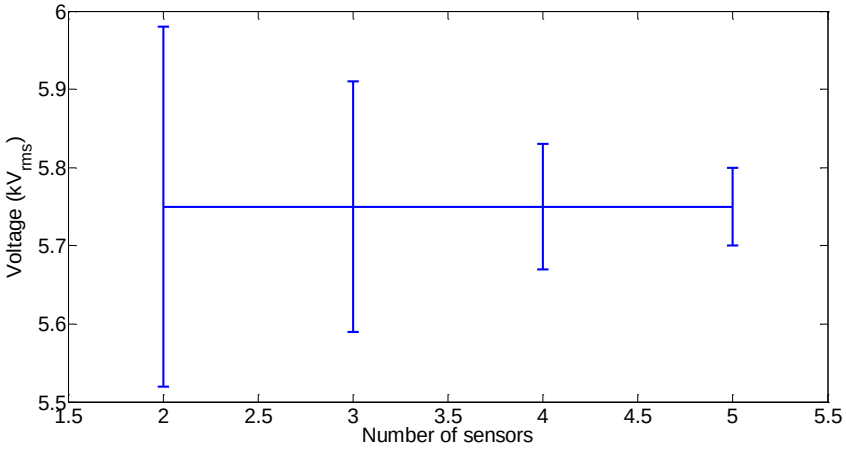

Fig. 6.8: The maximum deviation in the calculated voltage using the curve fitting method is shown as error bars for different number of points at which the electric field is measured (number of sensors).

profile information. In the reported measurements of this section, the values of d and V_0 were assumed to be the unknown. In order to find the unknown values, the electric field profile was measured using the sensor at different height levels. The distance of the sensor to the conductor was assumed to be known. Then, using curve fitting on the measured electric field profile, the unknown values were calculated. The calculated unknown d and V_0 agrees with the expected values reported in Table 6.3.

6.2 Detection of Defects in Insulators

Different types of insulators installed on transmission lines are porcelain, glass and polymeric insulators as shown in Fig. 6.9. Defects on these insulators differ depending on the type of insulator. Hence, the preferred defect detection method employed for each type of insulator is different. As an example, the glass insulators typically shatter under electrical or mechanical stress which is detectable by visual inspection.

The typical types of tests to detect the defection of the insulators are visual inspection, buzz test, resistance measurement, voltage measurement and electric field measurement. Other recently employed methods of inspection used for live line measurements include corona camera test, HF emission, acoustic emission and IR thermography. Although most of the defects are not visible, visual inspection is the most commonly used method for all types of insulators. Some methods such as buzz test, resistance measurement and voltage measurement require close inspection by an operator, hence increasing safety hazard. In these methods, the operator holds the measuring probes in contact with the insulators using a long hot-stick. The unconventional defect detection methods employ remote measurement, hence reducing the safety issues pertinent to close proximity with high voltage. These methods suffer from low accuracy caused by noise or interference, *e.g.* daylight interferes with corona camera visibility.

Currently, detecting the variation in the electric field surrounding a defected non-

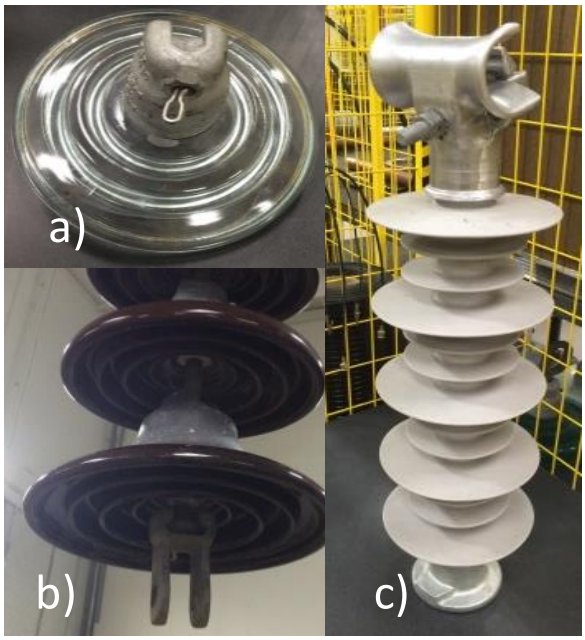

Fig. 6.9: Different types of insulators, a) glass, b) porcelain c) composite.

ceramic insulator is the most commonly used method for the inspection of composite insulators as the defect detection methods for composite insulators are still under study [63].The available electric field measurement probes used in detection of insulator defects measure the longitudinal electric field along the string of insulators. The measured electric field will be recorded and later compared to the expected electric field of a healthy insulator string. The measured electric field surrounding the defected string shows deviation from the expected graph [5, 19–21, 25, 64]. The available electric field probes currently employed in defect detection of insulators are probes that are either active electric field sensors attached to the end of a hot stick or optical probes connected to an analyzing system through fiber optics.

6.2.1 Detection of defects by Measuring the Electric-Field Along an Insulator

In this section, the simulation and the measurement results of employing the proposed electric field sensor for detecting defects on an insulator are reported. The electric field profiles along a healthy and defected insulator are compared. In composite insulators, a typical defect is a result of a crack inside the insulator rod (made of fiberglass) caused by electrical or mechanical stress. The humidity of air accumulated inside the crack results in a conductive path along the rod. In order to simulate the conductive path in the measurements, a piece of copper tape is attached to the surface of the insulator.

Measurement Results

A nonconductive platform is employed in moving the sensor along the insulator. The sensor and the interrogator antenna are mounted on this platform with a distance of 60 cm between the antennas. The platform moves the sensor along an energized composite insulator to measure the resonance frequency variation of the sensor caused by the inducing voltage. The conductor connected to one side of the insulator is energized with a voltage of $6400\,\mathrm{V}_{rms}$ while the other side of the insulator is grounded. The electric field profile is then measured along the insulator for two cases of healthy and defected insulator using the recorded results from the sensor. The platform locates the sensor at steps 1.5 cm apart and the AC electric field at each step is recorded for a length similar to the results reported in Fig. 6.6. Copper tape is attached over three sheds of the insulator (shown in Fig. 6.10) to simulate a defect along the insulator rod. The insulator used in the measurements is 43 cm long and includes 9 sheds. The measurement is conducted along a reference line in parallel to the insulator. The sensor moves along the reference line such that there is 1 cm gap between the outer body of the sensor and the tip of the sheds.

The electric field profile along the insulator for two cases of with and without defects

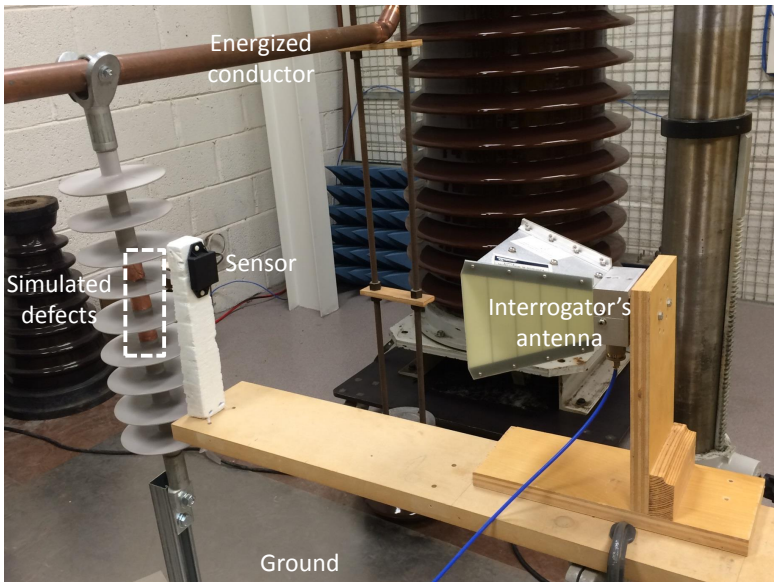

Fig. 6.10: Picture of the measurement setup employed for detection of defects consists of the sensor clamped on a nonconductive platform and close to the insulator with the copper tape attached over the insulator rod to simulate a defect.

is shown in Fig. 6.11. The defect is simulated using copper tape over the outer body of the insulator rod which electrically connects 4 sheds of the insulator. The sensor moves from the grounded side of the insulator towards the energized conductor. The sheds are numbered respectively with the first shed on the ground side and the 9th shed on the conductor side. The horizontal axis, *i.e.* shed number, in Fig. 6.11 defines the location of the top plate (containing the varactors) of the sensor at each measuring point. The defect (copper tape) is electrically connecting sheds 4 to 7. The measurement results reported in Fig. 6.11 shows a deviation of the measured electric field in case of the defected insulator from the case of a healthy insulator in close proximity to the defect location.

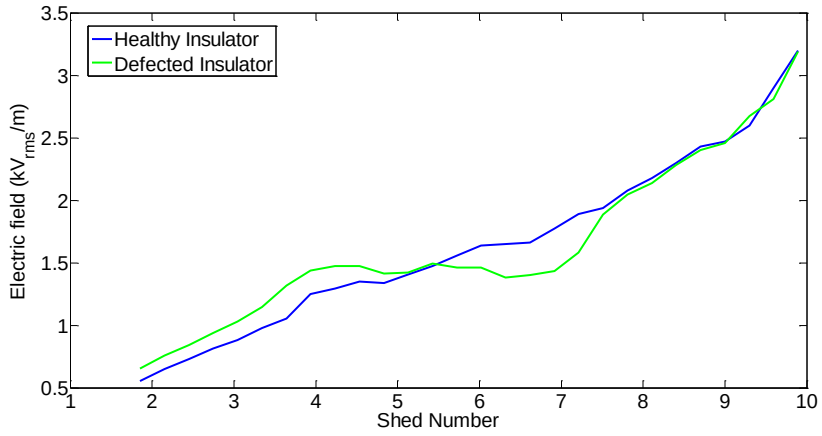

Fig. 6.11: The measurement results of the electric field profile along the insulator in two cases of with and without defects. A copper tape along three sheds on the insulator simulates a crack in the insulator's rod. The sheds are numbered 1 to 9 from the ground to the other side of the insulator.

Simulation Results

The finite element simulation results of the insulator with and without a conductive surface similar to the measurement setup are shown in Fig. 6.12. The 3D geometry of the insulator connected to a voltage line and placed above the ground is built in Comsol (shown in Fig. 6.13). The simulated sensor is moved along a line in parallel to the insulator and the electric field above the sensor is measured with and without the defect. The copper tape used as the defect in measurements is simulated by defining a conductive surface over the three sheds (number 4 to 7).

The simulation results shown in Fig. 6.11 and the measurement results shown in Fig. 6.12 are similar in that maximum electric field surrounding the defected insulation is at shed 4 and the minimum is at shed 7. Also, the magnitude of deviation of electric field close to the defect location in both experimental and simulation results is large compared to the noise of the system. Therefore, the presence of a crack inside an insulator is expected to be observable using the electric field sensor. However, there are significant differences

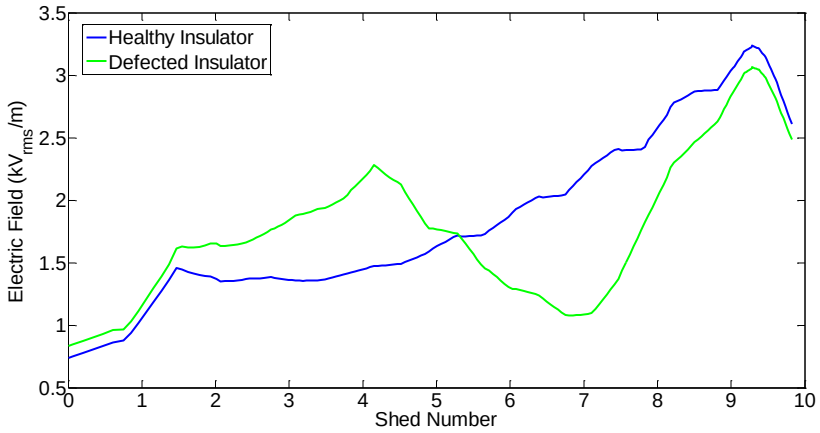

Fig. 6.12: The finite element simulation result of electric field along the insulator in two cases of without defects and with conductive surface along three sheds on the insulator simulating a crack in the insulator's rod.

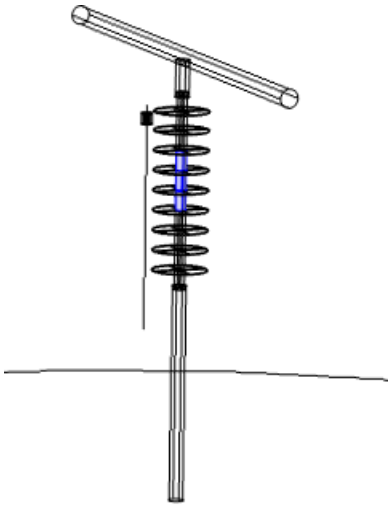

Fig. 6.13: The 3D simulated geometry of the insulator over ground in Comsol. The sensor is moved along the line in parallel to the insulator.

between the experimental and simulation results. Comparing the results of measurement and simulation shows a difference in the electric field profile magnitude. The parameters that affect the measurement results (Fig. 6.11) and are not considered in the simulation are the presence of sensor antenna, interrogator antenna, and other conductive surfaces in close proximity of the insulator which influence the distribution of the electric field. Further,The electric field profile surrounding the insulator consists of a combination of the electric field components in directions of x, y and z coordinates. However, the electric field profile derived by measurement is more influenced by the z component of the electric field than the electric field in other directions assuming z direction is along the insulator rod, because the mapping graph in Fig. 4.11 is used to calculate the RMS value of the electric field from the measured resonance frequency which was derived by measuring electric field consisting of only z component. Hence, the resonance frequency of the sensor in the measurement results is mainly influenced by the electric field component in the z direction while in the simulation results the electric field magnitude is influenced by all the electric field components (in x,y, and z direction) at each location. In summary, the simulation results does not include the elements that may have a significant influence on the actual fields.

6.2.2 Proposed Defect Detection Method Using Passive Electric-Field Sensor

The method employed in the detection of defects on composite insulators reported in the previous section requires close proximity of an operator to the high voltage apparatus in order to move the sensor along the insulator similar to the conventional insulator assessment techniques employing electric field measurement. In order to increase the safety of the workers, the passive wireless sensor is proposed to be permanently mounted in close proximity of the insulator and the electric field is measured remotely using the interrogation system. A number of these sensors must be mounted on an insulator to monitor the electric

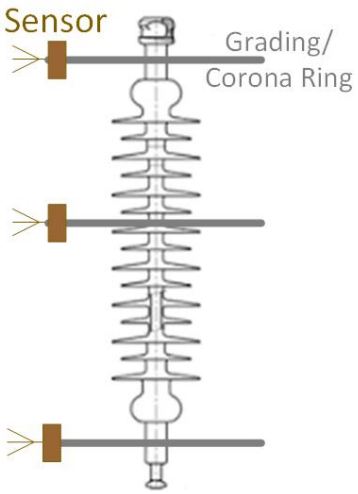

Fig. 6.14: The proposed insulation assessment method using the passive wireless sensor measuring the electric field surrounding an insulator.

field profile over the insulator. Since the voltage variation affects the electric field profile and correspondingly the electric field measured by the sensors surrounding an insulator, the defect detection method must be voltage-independent. Monitoring of the difference between the electric field measured by each two sensors and comparing with the difference in the case of a healthy insulator would provide the required voltage-independent information for defect detection. In order to permanently mount the sensors in close proximity of the insulator, the sensors can be mounted on corona/grading rings attached to the insulators. The corona/grading rings are available in different sizes and are used to reduce the density of the electric field surrounding an insulator. The rings can be employed in mounting the sensors on an insulator as shown in Fig. 6.14. The sensors can also be mounted over the insulators using nonconductive clamps.

6.3 Summary

Two potential applications of the passive wireless sensor for the measurement of electric field in the vicinity of high voltage apparatus were discussed in this chapter. The feasibility of a contactless voltage measurement method employing the passive wireless electric field sensor for the measurement of the medium or high voltage is verified by measurement results in this chapter. Further, a distance-independent technique is proposed using an array of the electric field sensors. The results are derived after calibrating the sensor by applying known voltages to the conductor over ground and deriving the graph of electric field variation as a function of the measured resonance frequency. The voltage of the conductor inducing the measured electric field is then calculated for known distances of the conductor and the sensor to the ground. Demonstrating the feasibility of the contactless voltage measurement approach, a self-calibrating method is also proposed and verified by measurement using an array of three electric field sensors. The measured electric field surrounding the sensors are used for the calculation of the voltage and the distance of the conductor to the ground.

In the second application, the sensor was employed in the detection of defects on a composite insulator. The measurements of the electric field surrounding a defected and a healthy insulator are compared. The results demonstrate that a significant deviation in the measured electric field occurs close to the defected string of the insulator. By mounting a number of passive wireless sensors on corona/grading rings attached to the insulator, defects on an insulator can be detected remotely. The remote measurement method significantly reduces the safety hazards pertinent to the available defect detection methods which require close proximity of line workers with high voltage.

Chapter 7

Concluding Remarks

In this thesis, the design, fabrication and testing of a passive, wireless electric field sensor has been presented. This sensor is employed in electric field measurements in the vicinity of high voltage apparatus and is potentially an alternative to the bulky measurement devices which require direct electrical attachment to the high voltage apparatus. The sensor is passive which eliminates the need for batteries and the remote interrogation provides the required safety clearance distance from the high voltage apparatus. The proposed sensor is applicable in remote measurement of medium or high voltage and detection of defects in the insulators.

The proposed electric field sensor is a resonator with variable resonance frequency. The designed sensor is a cavity resonator coupled to varactors that are voltage-dependent capacitive elements. The bias voltage over the terminals of the varactors is induced by the external electric field surrounding the sensor. The variation of the external electric field changes the equivalent capacitance of the varactors and correspondingly the resonance frequency of the sensor. A pulse of radio frequency (RF) signal in the ISM band of 2400MHz to 2500 MHz range is transmitted to the resonator. The sensor resonates at its natural frequency and re-emits a ring-back which will be captured by the interrogation system.

The recorded ring-back is analyzed to identify the resonance frequency of the sensor at that instant. A repetition of these pulses at a rate up to 2.5 MHz is generated and transmitted by the interrogation system resulting in a high sampling rate of the induced electric field emanating from the high voltage apparatus.

The proposed passive, wireless sensor is a novel electric field measuring sensor that increases the safety of the operators in high voltage applications by providing remote and contactless measurements. Measurement results captured using the designed sensor and the prototype of the interrogation system have proven the applicability of the sensors in the wireless measurement of voltage and detection of defects inside the insulators. As one application of the sensor, the voltage of a single phase conductor above ground was measured. In the measurements, the sensor is placed in multiple locations beneath the conductor and the electric field at each location is used to derive the electric field profile surrounding the conductor. A method was proposed to translate the electric field profile to the voltage of the conductor.

Defect detection of insulators is proposed as another application for the proposed sensor. The sensor is moved along an insulator with and without a defect in order to measure the electric field profile surrounding the insulator. The graph of the electric field profile surrounding a defected insulator shows a deviation from the profile in case of a healthy insulator, hence showing the presence of a defect.

7.1 Future Work

The measurement results presented in this thesis demonstrate the functionality of the proposed sensor and the interrogation system. The sensor and the interrogation system can be improved in both hardware and software. Further investigation is required to improve the efficiency and accuracy of the proposed sensor for high voltage applications. In this section, further studies are suggested to improve the sensor functionality and extend the

applications of the senor in high voltage measurements.

7.1.1 Hardware and Software Improvements

The proposed passive, remote electric field measurement method was verified using prototype models of the sensor and an interrogation system which require further improvements to increase the speed and accuracy of the measurements. The interrogation system in Fig. 4.2 is based on recording the ring backs on a fast sampling rate oscilloscope. The recorded data is then transferred to a computer to be analyzed. The size and the cost of the interrogation system will be significantly reduced by replacing the oscilloscope and the computer with a fast sampling rate processor such as an FPGA. Employing the processor will also increase the speed of the measurements such that real-time electric field and voltage measurement and monitoring will become feasible.

The sensor structure requires further improvement such as replacing the commercialized antenna used for the sensor. The antenna is replaceable by an antenna embedded to the sensor structure. Additionally, the sensor consisting of the resonator and the antenna can be machined out of solid copper to reduce the inaccuracies caused by soldering.

The proposed sensor structure is adaptable to different measurement scenarios. Some changes are required to adjust the sensor to different environments. As an example, changing the internal lumped elements inside the resonator, *i.e.* the resistors in parallel with the varactors, will change the measurable (dynamic) range. Another environmental effect that is required to be considered in future measurements in order to adapt the results to different measurement scenarios is the temperature variations. The effect of temperature on the sensor can be monitored by a passive, wireless temperature sensor mounted close to the electric field sensor. The temperature sensor is a cavity resonator with a different resonance frequency range from the electric field sensor. The variation in the temperature changes the size of the cavity and accordingly the resonance frequency of the temperature sensor. The

sensor is interrogated by the same interrogation system sensing two different RF pulses to interrogate the electric field and the temperature sensors simultaneously. The information of the temperature is then employed in correcting the measurement errors of the electric field sensor due to the temperature variations.

The current interrogation system is capable of interrogating one sensor which limits the application of the proposed sensor. Simultaneous interrogation of multiple sensors with different resonance frequencies requires modifying the interrogation system by adding a frequency hopping method to the transceiver. Frequency hopping is a method widely used in radio frequency transceivers in order to reduce the interference of the RF signal devices operating in the interrogator's frequency band. Additionally, the ISM band regulations allow a wider power range for transmitters with frequency hopping method as compared to those operating with a fixed frequency. Higher transmitting power of the interrogation system will accordingly increase the interrogation distance.

Since the resonance frequency of the sensor is power dependent (discussedd in Section 4.4.1), determining the power consumed by the resonator at the initial stage of the measurements is important in choosing the mapping graph of resonance frequency to electric field. The software developed for analyzing the recorded ring backs can be extended to initialize the measurement process by transmitting impulses and analyzing the delay in capturing the re-emitted signal. This method is generally employed in radar systems to locate an object. The delay can be used in estimating the distance between the sensor and the interrogation system. The distance of the resonator from the interrogation antenna defines the power received at the resonator.

7.1.2 Improving the Sensor for High Voltage Measurements

The measurement results obtained from the proposed sensor and the interrogation system proves the capability of the sensor in contactless voltage measurement and detection of

insulation defects. The interrogation system can be implemented on a standalone, integrated circuit enabling simultaneous interrogation of multiple sensors. Furthermore, the remote and distributed measurement of voltage and real-time detection of defects in the insulators will be feasible by providing a network connection among the interrogation systems. The network connection transfers the data captured from the sensors in a wide-area power system to a control and monitoring center that is responsible for decision making in power systems.

The proposed electric field sensor in this thesis has been proved to be applicable in remote voltage measurement of single phase conductors. However, the transmission and distributions lines in power systems consist of three phase bundles. In order to use the proposed sensor in power systems, a major challenge is to adapt the voltage measuring sensor for the measurement of the voltage of a three phase line using the induced electric field profile. Multiple sensors must be employed to exclude the effect of the two other phases. A calculation method must be further developed to derive the phase voltage using the measured electric field profile surrounding three phase conductors using the passive electric field sensors.

Another application of the proposed electric field sensor in high voltage that is verified by measurement results (in Section 6.2) is the detection of the defects inside an insulator. The measurement method requires close proximity of an operator handling the hotstick that holds the sensor. In the proposed method, the electric field sensor is moved along an insulator to measure the profile of the electric field surrounding the sensor. The difference between the profiles of a defected and a healthy insulator indicates the presence of a defect. In order to provide the safety of the operators conducting the measurements, an alternative method to moving the sensor along the insulator is proposed. The sensors can be mounted on the insulators permanently using corona/grading rings. The difference between the electric field values measured at any two sensors on the insulatorratio of the change in electric field values measured for the cases of the healthy and defected insulators are compared. The

change in the ratio of the difference between the measured electric field values indicates the presence of a defect. The electric field measured on the insulators is dependent on the voltage of the conductors connected to the insulators. Hence, using the ratio of the difference between the measured electric field values instead of comparing the actual value of electric field will eliminate the need for knowing the inducing voltage on the conductor over the insulator. The efficacy of the proposed method requires further investigation since the permanent presence of a conductor in close proximity to the high voltage devices is not desirable.

References

[1] F. Delea, J. Casazza, *Understanding Electric Power Systems:An Overview of the Technology, the Marketplace, and Government Regulation.* Wiley-IEEE Press, 2010.

[2] V. Gungor, B. Lu, and G. Hancke, "Opportunities and challenges of wireless sensor networks in smart grid," *IEEE Trans. Ind. Electron.*, vol. 57, no. 10, pp. 3557–3564, Oct 2010.

[3] A.K.M. Baki, "Continuous monitoring of smart grid devices through multi protocol label switching," *IEEE Trans. Smart Grid*, vol. 5, no. 3, pp. 1210–1215, May 2014.

[4] Y. C. Chen, C. rong Li, X. Liang, and S. Wang, "The influence of water and pollution on diagnosing defective composite insulator by electric field mapping," in *Eleventh Int. Symposium on High Voltage Engineering*, vol. 4, 1999, pp. 345–348 vol.4.

[5] G.H. Vaillancourt, S. Carignan, and C. Jean, "Experience with the detection of faulty composite insulators on high-voltage power lines by the electric field measurement method," *IEEE Trans. Power Del.*, vol. 13, no. 2, pp. 661–666, Apr 1998.

[6] B. Zemljaric, "Calculation of the connected magnetic and electric fields around an overhead-line tower for an estimation of their influence on maintenance personnel," *IEEE Trans. Power Del.*, vol. 26, no. 1, pp. 467–474, Jan 2011.

[7] C.A. Gerrard, J.R. Gibson, G.R. Jones, L. Holt, and D. Simkin, "Measurements of power system voltages using remote electric field monitoring," *IEE Proceedings- Generation, Transmission and Distribution*, vol. 145, no. 3, pp. 217–224, May 1998.

[8] C. E. Lin, J.-B. Wei, C.-L. Huang, and C.-J. Huang, "A new model for transformer saturation characteristics by including hysteresis loops," *IEEE Transactions on Magnetics*, vol. 25, no. 3, pp. 2706–2712, May 1989.

[9] E. E. Barkat and D. E. Hirst, "Susceptibility of 3-phase power systems to ferro-nonlinear oscillations," *Proceedings of the Institution of Electrical Engineers*, vol. 126, no. 12, pp. 1295–1300, 1979.

[10] F. Y. Chu, "SF6 decomposition in Gas-Insulated Equipment," *IEEE Transactions on Electrical Insulation*, vol. EI-21, no. 5, pp. 693–725, Oct 1986.

[11] R. Moghe, A.R. Iyer, F.C. Lambert, and D.M. Divan, "A low-cost wireless voltage sensor for monitoring MV/HV utility assets," *IEEE Trans. Smart Grid*, vol. 5, no. 4, pp. 2002–2009, July 2014.

[12] R. Moghe, A. Iyer, F. Lambert, and D. Divan, "A robust smart sensor for smart substations," in *IEEE Power and Energy Society General Meeting*, July 2012, pp. 1–8.

[13] M. A. Noras, "Solid state electric field sensor," in *ESA Annual Meeting on Electrostatics*, 2011.

[14] F. Rahmatian, and P.P. Chavez, "SF6-free 550 kV combined optical voltage and current transducer system," in *IEEE PES Transmission and Distribution Conf. and Expo.*, vol. 1, Sept 2003, pp. 379–382.

[15] M. Yazdani, D. J. Thomson, B. Kordi, International PCT PCT/CA2015/051 188, November 13, 2015.

[16] M. Yazdani, D.J. Thomson, and B. Kordi, "Wireless pulse echo interrogation of an ac electric potential resonator sensor," in *IEEE Int. Conf. on Industrial Technology*, March 2015.

[17] M. Yazdani, D. J. Thomson, B. Kordi, D. Swatek, "Calibration of passive wireless electric field sensor for the measurement of medium/high voltage," in *CIGRE Canada Conference*, August 31- September 2 2015.

[18] M. Yazdani, D. J. Thomson, and B. Kordi, "Passive wireless sensor for measuring ac electric field in the vicinity of high-voltage apparatus," *IEEE Transactions on Industrial Electronics*, vol. 63, no. 7, pp. 4432–4441, July 2016.

[19] G.H. Vaillancourt, J.P. Bellerive, M. St-Jean, and C. Jean, "New live line tester for porcelain suspension insulators on high-voltage power lines," *IEEE Trans. Power Del.*, vol. 9, no. 1, pp. 208–219, Jan 1994.

[20] G. V. D.H. Shaffner, D.L. Ruff, "Experience with a composite insulator testing instrument based on the electric field method," in *IEEE ESMO, 9th Int. Conf. on Transmission and Distribution Construction, Operation and Live-Line Maintenance Proc.*, 2000, pp. 318–327.

[21] G. Karady, "Electrical test methods for nonceramic insulators used for live line replacement," *IEEE Trans. Power Del.*, vol. 12, no. 2, pp. 965–970, Apr 1997.

[22] M. Passard, C. Barthod, M. Fortin, C. Galez, and J. Bouillot, "Design and optimization of a low-frequency electric field sensor using pockels effect," *IEEE Trans. Instrum. Meas.*, vol. 50, no. 5, pp. 1053–1058, Oct 2001.

[23] C. Han, F. Lv, C. Sun, and H. Ding, "Silica microwire-based interferometric electric field sensor," *Opt. Lett.*, vol. 40, no. 16, pp. 3683–3686, Aug 2015.

[24] N. Jaeger and F. Rahmatian, "Integrated optics Pockels cell high-voltage sensor," *IEEE Trans. Power Del.*, vol. 10, no. 1, pp. 127–134, Jan 1995.

[25] W. C. R. Zeng, Y. Zhang and B. Zhang, "Measurement of electric field distribution along composite insulators by integrated optical electric field sensor," *IEEE Trans. Dielectr. Electr. Insul.*, vol. 15, no. 1, pp. 302–310, February 2008.

[26] C. Volat, M. Jabbari, M. Farzaneh, and L. Duvillaret, "New method for in live-line detection of small defects in composite insulator based on electro-optic e-field sensor," *IEEE Trans. Dielectr. Electr. Insul*, vol. 20, no. 1, pp. 194–201, February 2013.

[27] M. Bernier, L. Duvillaret, G. Gaborit, A. Paupert, and J. L. Lasserre, "Fully automated e-field measurement system using pigtailed electro-optic sensors for temperature-dependent-free measurements of microwave signals in outdoors conditions," *IEEE Sensors J.*, vol. 9, no. 1, pp. 61–68, Jan 2009.

[28] B. Bahreyni, G. Wijeweera, C. Shafai, and A. Rajapakse, "Analysis and design of a micromachined electric-field sensor," *J. of Microelectromechanical Systems*, vol. 17, no. 1, pp. 31–36, Feb 2008.

[29] G. Wijeweera, B. Bahreyni, C. Shafai, A. Rajapakse, and D.R. Swatek, "Micromachined electric-field sensor to measure ac and dc fields in power systems," *IEEE Trans. Power Del.*, vol. 24, no. 3, pp. 988–995, July 2009.

[30] R.N. Dean and A. Luque, "Applications of microelectromechanical systems in industrial processes and services," *IEEE Trans. Ind. Electron.*, vol. 56, no. 4, pp. 913–925, April 2009.

[31] M. N. Horenstein and P. R. Stone, "A micro-aperture electrostatic field mill based on MEMS technology," *J. of Electrostatics*, vol. 5152, pp. 515 – 521, 2001, electrostatics 2001: 9th International Conference on Electrostatics.

[32] P. Yang, C. Peng, H. Zhang, S. Liu, D. Fang, and S. Xia, "A high sensitivity soi electric-field sensor with novel comb-shaped microelectrodes," in *16th Int. Solid-State Sensors, Actuators and Microsystems Conf. (TRANSDUCERS)*, June 2011, pp. 1034–1037.

[33] X. Chen, C. Peng, H. Tao, C. Ye, Q. Bai, S. Chen, and S. Xia, "Thermally driven micro-electrostatic fieldmeter," *Sensors and Actuators A: Physical*, vol. 132, no. 2, pp. 677 – 682, 2006.

[34] S. Ghionea, G. Smith, J. Pulskamp, S. Bedair, C. Meyer, and D. Hull, "Mems electric-field sensor with lead zirconate titanate (PZT)-actuated electrodes," in *IEEE Sensors J.*, Nov 2013, pp. 1–4.

[35] W. McNulty, "Voltage detection and indication by electric field measurement," *HD Electric Company*, 2011.

[36] M. Noras and A. Pandey, "Surface charge density measurements," *IEEE Ind. Appl. Mag.*, vol. 16, no. 4, pp. 41–47, July 2010.

[37] F. Yu, K.G Lyon, and E.C. Kan, "A novel passive RFID transponder using harmonic generation of nonlinear transmission lines," *IEEE Trans. Microw. Theory Techn.*, vol. 58, no. 12, pp. 4121–4127, Dec 2010.

[38] B. Colpitts and G. Boiteau, "Harmonic radar transceiver design: miniature tags for insect tracking," *IEEE Trans. Antennas Propag.*, vol. 52, no. 11, pp. 2825–2832, Nov 2004.

[39] I. Nassar, T. Weller, and J. Frolik, "A compact 3D harmonic repeater for passive wireless sensing," *IEEE Trans. Microw. Theory Techn.*, vol. 60, no. 10, pp. 3309–3316, Oct 2012.

[40] V. Viikari, H. Seppa, and D. Kim, "Intermodulation read-out principle for passive wireless sensors," *IEEE Trans. Microw. Theory Techn.*, vol. 59, no. 4, pp. 1025–1031, April 2011.

[41] V. Viikari, J. Song and H. Seppa, "Passive wireless sensor platform utilizing a mechanical resonator," *IEEE Sensors J.*, vol. 13, no. 4, pp. 1180–1186, April 2013.

[42] J. Song, N. Pesonen,H. Seppa and V. Viikari, "On the use of the intermodulation communication towards zero power sensor nodes," in *European Microwave Conf. (EuMC)*, Oct 2013, pp. 124–127.

[43] J. Chuang, D.J. Thomson, and G.E. Bridges, "Embeddable wireless strain sensor based on resonant RF cavities," *Review of Scientific Instruments*, vol. 76, no. 9, pp. 094 703–094 703–7, Sep 2005.

[44] D. J. Thomson, D. Card, and G.E. Bridges, "RF cavity passive wireless sensors with time-domain gating-based interrogation for SHM of civil structures," *IEEE Sensors J.*, vol. 9, no. 11, pp. 1430–1438, Nov 2009.

[45] P. Chen, S. Saati, R. Varma, M.S Humayun, and T. Yu-Chong, "Wireless intraocular pressure sensing using microfabricated minimally invasive flexible-coiled lc sensor implant," *J. of Microelectromechanical Systems*, vol. 19, no. 4, pp. 721–734, Aug 2010.

[46] F. Gattiker, F. Umbrecht, J. Neuenschwander, U. Sennhauser, and C. Hierold, "Novel ultrasound read-out for a wireless implantable passive strain sensor (WIPSS)," *Sensors and Actuators A: Physical*, vol. 145146, pp. 291 – 298, 2008.

[47] S. Bouaziz, F. Chebila, A. Traille, P. Pons, H. Aubert, and M. Tentzeris, "Novel microfluidic structures for wireless passive temperature telemetry medical systems using radar interrogation techniques in ka-band," *IEEE Antennas Wireless Propag. Lett.*, vol. 11, pp. 1706–1709, 2012.

[48] Y. Zhao, Y. Li, B. Pan, S.-H. Kim, Z. Liu, M. M. Tentzeris, J. Papapolymerou, and M. G. Allen, "RF evanescent-mode cavity resonator for passive wireless sensor applications," *Sensors and Actuators A: Physical*, vol. 161, pp. 322 – 328, 2010.

[49] Q Fu, J. Wang, D. Zhou, and W. Luo, "Passive wireless SAWR sensor system model including the effects of antenna distances," *Sensors and Actuators A: Physical*, vol. 150, no. 1, pp. 151 – 155, 2009.

[50] S. Bhadra, W. Blunt, C. Dynowski, M. McDonald, D. Thomson, M. Freund, N. Cicek, and G. Bridges, "Fluid embeddable coupled coil sensor for wireless pH monitoring in a bioreactor," *IEEE Trans. Instrum. Meas.*, vol. 63, no. 5, pp. 1337–1346, May 2014.

[51] W.-E. Bulst, G. Fischerauer, and L. Reindl, "State of the art in wireless sensing with surface acoustic waves," *IEEE Trans. Ind. Electron.*, vol. 48, no. 2, pp. 265–271, Apr 2001.

[52] K.G. Ong, C.A. Grimes, C.L. Robbins and R.S. Singh, "Design and application of a wireless, passive, resonant-circuit environmental monitoring sensor," *Sensors and Actuators A: Physical*, vol. 93, no. 1, pp. 33 – 43, 2001.

[53] S. Bhadra, C. Dynowski, W. Blunt, M. McDonald, D.J. Thomson, M. Freund, N. Cicek, G.E. Bridges, "Wireless passive sensor for pH monitoring inside a small bioreactor," in *IEEE Int. Instrumentation and Measurement Technology Conf., I2MTC*, May 2013, pp. 276–279.

[54] M. Nowak, N. Delorme, and F. Conseil, G. and Jacquemod, "A novel architecture for remote interrogation of wireless battery-free capacitive sensors," in *13th IEEE Int. Conf. on Electronics, Circuits and Systems, ICECS*, Dec 2006, pp. 1236–1239.

[55] B.E. Horton, S. Schweitzer, A.J. DeRouin, and Keat Ghee Ong, "A varactor-based, inductively coupled wireless pH sensor," *IEEE Sensors J.*, vol. 11, no. 4, pp. 1061–1066, April 2011.

[56] M.P. Robinson, and J. Clegg, "Improved determination of Q-factor and resonant frequency by a quadratic curve-fitting method," *IEEE Trans. Electromagn. Compat.*, vol. 47, no. 2, pp. 399–402, May 2005.

[57] Y. Yan, Z. Zeng, C. Chen, H. Jiang, Z. Chang, D.M. Karabacak, and M.A.P. Pertijs, "An energy-efficient reconfigurable readout circuit for resonant sensors based on ring-down measurement," in *IEEE Sensors J.*, Nov 2014, pp. 221–224.

[58] M. Ghafourian, G. E. Bridges, A. Zeidabbadi-Nezhad and D. J. Thomson, "Wireless overhead line temperature sensor based on RF cavity resonance," *Smart Materials and Structures*, vol. 22, no. 7, 2013.

[59] J.A. Navarro, and K. Chang, "Varactor-tunable uniplanar ring resonators," *IEEE Trans. Microw. Theory Techn.*, vol. 41, no. 5, pp. 760–766, May 1993.

[60] A. R. Johnston, and H. Kirkham, "A miniaturized space-potential dc electric field meter," *IEEE Trans. Power Del.*, vol. 4, no. 2, pp. 1253–1261, Apr 1989.

[61] F. Rahmatian, J. H. Gurney, and J. A. Vandermaar, "Portable 500kV optival voltage transducer for on-site calibration of high voltage transformers without de-energization," in *CIGRE General Session 41*, September 2002.

[62] M. A. Noras, "Non-contact surface charge/voltage measurements capacitive probe - principle of operation," *Trek Application Note*, no. 3001, 2002.

[63] R. Lings, "Identifying defects in polymer insulators that are detrimental to live working: Technical pogress," EPRI, Palo Alto, CA, Technical Progress July, 2002.

[64] C. Volat, M. Jabbari, M. Farzaneh, and L. Duvillaret, "New method for in live-line detection of small defects in composite insulator based on electro-optic e-field sensor," *IEEE Trans. Ind. Electron.*, vol. 20, no. 1, pp. 194–201, February 2013.

Appendix A

Detailed Elements of Interrogator

The elements used in the interrogation system are shown in the block diagram of Fig. A.1. See the next page.

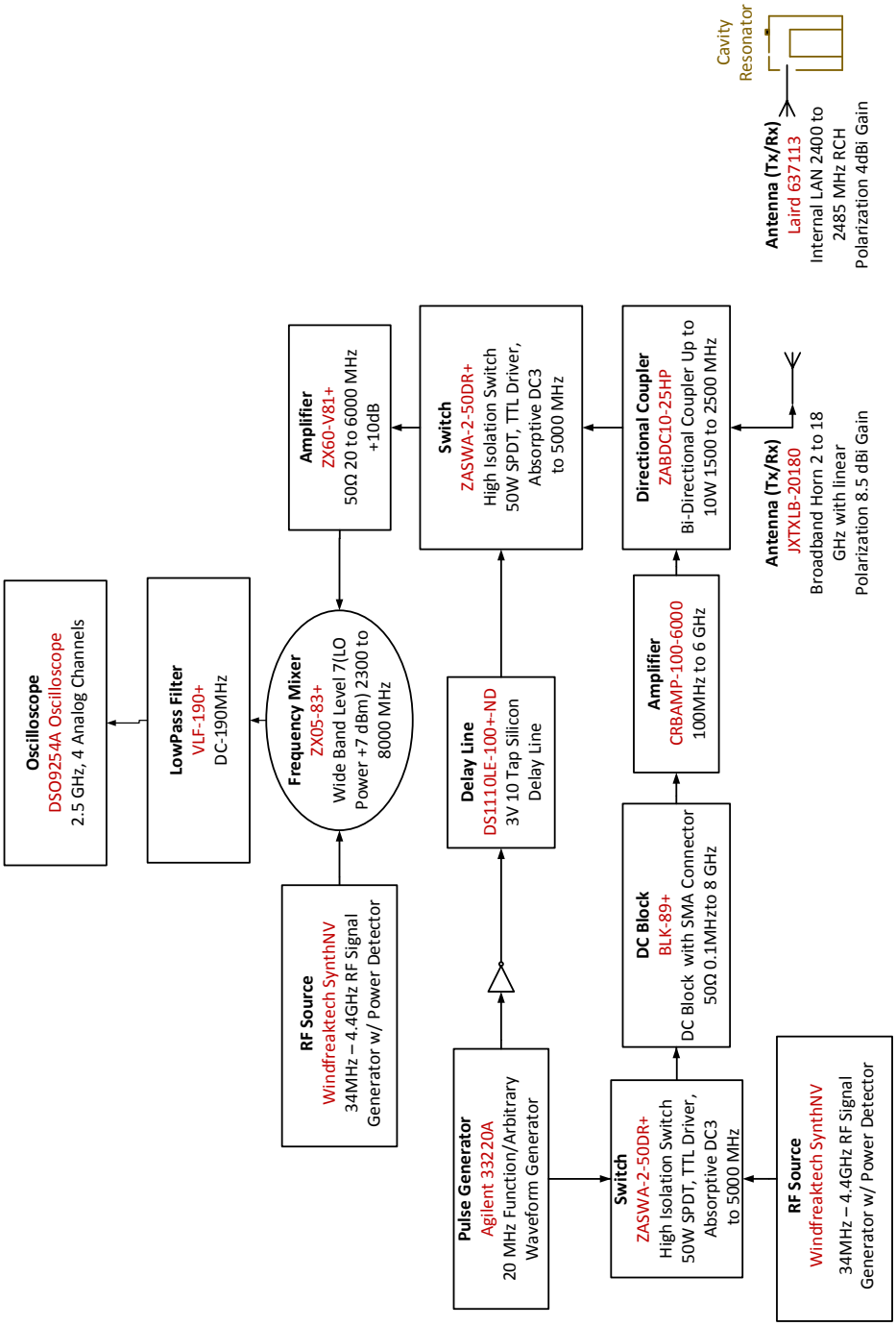

Fig. A.1: Detailed block diagram of the elements used in the interrogation system.